The Pennsylvania State University

The Graduate School

College of Engineering

DEVELOPMENT OF A DYNAMIC CALIBRATION TARGET FOR THROUGH-WALL AND THROUGH-RUBBLE MOTION SENSING DOPPLER RADAR

A Thesis in

Electrical Engineering

by

Michael J. Harner

Submitted in Partial Fulfillment
of the Requirements
for the Degree of

Master of Science

May 2018

The thesis of Michael Harner was reviewed and approved* by the following:

Ram M. Narayanan
Professor of Electrical Engineering
Thesis Advisor

Julio V. Urbina
Professor of Electrical Engineering

Kultegin Q. Aydin
Professor of Electrical Engineering
Head of the Department of Electrical Engineering

*Signatures are on file in the Graduate School

ABSTRACT

Through-wall/through-barrier motion sensing systems are becoming increasingly important tools to find people hidden behind barriers and under rubble. The sensing performance of these systems is best determined with calibration targets. The effectiveness of various dynamic calibration targets that emulate human respiration, heart rate, and other body motions are analyzed. Potential advantages of these targets are in their reproducibility and accuracy in support of calibration methods for human detection testing in through-wall and through-rubble situations. The three targets examined in this thesis possess spherical polyhedral geometries. Spherical geometries were selected due to their isotropic radar cross section characteristics, which provides for consistent radar returns independent of orientation of the radar transceiver relative to the test target. The ability to use a target that is aspect independent is favorable during the calibration process. Furthermore, rather than using a traditional, static calibration sphere, a dynamic, sphere-like device offers the ability to resemble motions of the human body. This motion enables numerous types of Doppler testing that are impossible in a static calibration target. Monostatic RCS simulations at 3.6 GHz are documented for each geometry. The results provide a visual way of representing the effectiveness of each design as a dynamic calibration target for human detection purposes.

TABLE OF CONTENTS

List of Figures v

List of Tables vii

Acknowledgements viii

Chapter 1 – Introduction and Motivation 1

Chapter 2 – Background 3

2.1 Radar Cross Section 3
2.2 Variations in Human RCS 4
2.3. The Sphere as a Calibration Device 10
2.4. Emulating Human RCS 17

Chapter 3 – Simulation Process 19

3.1 Parameters 19
3.2 Creating the Models 20
3.3 Results 20

Chapter 4 – Prototype 37

4.1 Overview 37
4.2 Design 37
4.3 3-D Printing and Coating 39
4.4 Test Setup 45
4.5 Experimental Approach 46

Chapter 5 – Concluding Remarks 56

Bibliography 59

LIST OF FIGURES

Figure 1. Monostatic RCS analysis of a standing human.

Figure 2. Normalized monostatic RCS of a sphere as a function of radius

Figure 3. Three different types of spherical polyhedra

Figure 4. Tetrahedron geometry

Figure 5. Hexahedron geometry

Figure 6. Octahedron geometry

Figure 7. Dodecahedron geometry

Figure 8. Icosahedron geometry

Figure 9. Monostatic RCS results for the contracted tetrahedron at 3.6 GHz

Figure 10. Monostatic RCS results for the expanded tetrahedron at 3.6 GHz

Figure 11. Monostatic RCS results for the contracted hexahedron at 3.6 GHz

Figure 12. Monostatic RCS results for the expanded hexahedron at 3.6 GHz

Figure 13. Monostatic RCS results for the contracted octahedron at 3.6 GHz

Figure 14. Monostatic RCS results for the expanded octahedron at 3.6 GHz

Figure 15. Monostatic RCS results for the contracted dodecahedron at 3.6 GHz

Figure 16. Monostatic RCS results for the expanded dodecahedron at 3.6 GHz

Figure 17. Monostatic RCS results for the contracted icosahedron at 3.6 GHz

Figure 18. Monostatic RCS results for the expanded icosahedron at 3.6 GHz

Figure 19. SolidWorks CAD model of the octahedron prototype

Figure 20. 1 of 8 face pieces for the octahedron prototype

Figure 21. Central sphere that interconnects all of the eight face pieces

Figure 22. Central sphere showing interconnect-ability with dowel rods

Figure 23. After result of splitting the face piece in half for 3-D printability

Figure 24. Two halves of the 3-D printed face part

Figure 25. Resulting face piece after assembling two halve pieces together.

Figure 26. After result of splitting central connecting object in two halves

Figure 27. Two halves of the 3-D printed central connector piece

Figure 28. Down range picture of the experimental setup used in the anechoic chamber

Figure 29. The two ϕ-cuts used during data collection. For both $\phi = 0°$ (left) and $\phi = 45°$ (right) a full 360° revolution was made around the θ-axis. Each was done in both the contracted and expanded state.

Figure 30. Normalized monostatic RCS of the target in its contracted state at $\phi = 0°$.

Figure 31. Normalized monostatic RCS of the target in its contracted state at $\phi = 45°$.

Figure 32. Normalized monostatic RCS of the target in its expanded state at $\phi = 0°$.

Figure 33. Normalized monostatic RCS of the target in its expanded state at $\phi = 45°$.

Figure 34. Comparison of experimental and simulated RCS in the expanded state at $\phi = 0°$.

Figure 35. Comparison of experimental and simulated RCS in the expanded state at $\phi = 45°$.

Figure 36. Raw RCS magnitudes when the target is in the expanded state at $\phi = 0°$.

Figure 37. Raw RCS magnitudes when the target is in the expanded state at $\phi = 45°$.

LIST OF TABLES

Table 1. An analysis on the heights of the human test subjects.

Table 2. An analysis on the weights of the human test subjects.

Table 3. An analysis on the BMI indices of the human test subjects.

Table 4. Data from test subjects who best-represented the average male and female adult.

ACKNOWLEDGEMENTS

I would like to thank my parents – Heather and Keith Phillips and Michael Harner Sr. – for all of their hard work and support throughout my life as well as my uncle – Don Mitchell – for first introducing me to Electrical Engineering. I would also like to thank Dr. Ram Narayanan for all of his guidance and giving me the opportunity to further my education. I would also like to thank all of my fellow lab mates who have helped me in various ways over the past two years – Matthew Brandsema, Marc Navagato, Joe O'Donnell, Logan Hall, and Sonny Smith. I would also like to thank Dr. Julio Urbina for taking the time to serve on my committee.

Finally, I would like to thank Nicholas Paulter and John Jendzurski of the National Institutes of Standards and Technology (NIST) for their guidance and mentorship during the research. This project was supported by NIST Grant # 70NANB16H023.

The findings and conclusions do not necessarily reflect the view of the funding agency.

Chapter 1 – Introduction and Motivation

Through-wall and through-rubble motion sensing Doppler radar systems have proven to be effective tools for the detection of humans in applications such as anti-terrorism, law enforcement, and calamitous events, such as earthquakes and landslides. Radar calibration targets emulating human breathing and heartbeat are useful for the testing and optimization of these systems in realistic scenarios.

The ideal calibration target must have two important attributes: (1) possess a radar cross section (RCS) close to that of a human, and (2) present essentially a constant RCS at all viewing angles. The aspect independence requirement stated in (2) is crucial because the calibration target may move, rotate, or otherwise be displaced during testing, but must nevertheless present a constant RCS at all viewing angles to maintain the accuracy of the calibration procedure. The ideal geometry for a calibration target is a sphere. What makes this geometry advantageous is the fact that its RCS is constant at any and all viewing angles. The scattering pattern of a sphere remains the same regardless of the illumination angle. By knowing exactly what return to expect, the calibration process becomes much more simplified. By expanding and contracting a calibration sphere radially in all directions, the sphere can be used to mimic human respiration and heartbeat. If the sphere is made with an appropriate diameter, such that it presents a radar signature similar to that of a human, then the radar return will be nominally the same for the target as it is for a human. To achieve such a feat, there must be a clear understanding of a human body's radar signature. There are numerous factors that go in to generating such a signature and the simulations are computationally intensive owing to the complex structure of the human body.

The following sections of this study are organized as follows. Chapter 2 discusses theoretical principles of radar cross section and how different target geometries affect backscatter during testing. Chapter 3 discusses the methodology used to simulate various scenarios in an electromagnetic computation software. Chapter 4 describes the finished prototype along with an analysis of the results. In Chapter 5, the study is concluded and we describe future goals for our work.

Chapter 2 – Background

1. Radar Cross Section

Radar cross section (RCS) plays a very important role in the analysis of different targets and systems. In general, RCS is a measure of how well a target reflects energy back towards a transmitting radar. Thus, it can be thought of as a measure of how visible a target is. The RCS can be thought of as a product of three factors: (1) projected cross section, (2) reflectivity, and (3) directivity [1]. Reflectivity relates to the scattering properties of the target; more specifically, how much incident power is reradiated from the target upon incidence. The directivity is a ratio of reradiated power scattered back towards the radar in comparison to the amount that would have scattered back towards the radar had the target been an isotropic radiator. The RCS, different from the geometric area of a target, is represented in meters squared (m^2). Visually, a target's RCS can be thought of as being equivalent to the cross-sectional area of a PEC sphere that reflects the same amount of energy back towards the radar. For example, a bird with an RCS of 0.01 m^2 will reflect the same amount of energy back towards the radar as a PEC sphere with a geometrical, cross-sectional area of 0.01 m^2 (i.e. diameter of 11 cm). The formal definition for radar cross section is defined as

$$\sigma = \lim_{r \to \infty} 4\pi r^2 \frac{|E_s|^2}{|E_i|^2} \tag{2.1}$$

where r is the distance between the radar and the target and E_i and E_s represent the incident and scattered electric fields, respectively [2]. In regards to the development of our calibration target, it is essential to understand the RCS of humans. Even further, we would like to know the RCS of

a breathing torso. If this can be achieved, it will be nearly impossible to distinguish between our calibration target and a human being, from the radar's perspective.

2. Variations in Human RCS

The human body's RCS is highly variable and full of complexities. The reason for such variability is largely due to the geometry and composition of the human body. A full 360-degree scan of any person will show jaggedness and numerous protrusions that will, in turn, produce a very complicated scattering pattern. In addition to the irregular shape, the body also possesses several dielectrics at different locations which can greatly attenuate incident energy. Overall, the many elements combine together to form a cross section that is dependent on body position, stance, and transmitting and receiving angles.

2.2.1 Dielectric Properties of the Human Body

The first layer of the human body that comes into contact with the radar's transmitted energy is the skin. With a very high dielectric constant of approximately 40.9, the skin layer tends to reflect most of the incoming energy [3]. Any remaining energy that passes through the skin will next come into contact with the fat layer, followed by the muscle layer. Body fat and muscle tissue have dielectric constants of about 5.4 and 54.8, respectively [3]. Due to the low dielectric properties of body fat, radar backscatter can sometimes be impacted by areas with high fat content. Any remaining energy that reaches the low-loss fat layer tends to be reflected. This reflection causes a phase-shift in the backscattered energy which, in turn, can cause destructive interference among the energy being backscattered from the skin layer. A person with high body fat percentage will present a thicker layer of fat and, thus, give off weaker returns than that of

someone with less body fat. This phenomenon is only prevalent when using frequencies below 1.2 GHz [3].

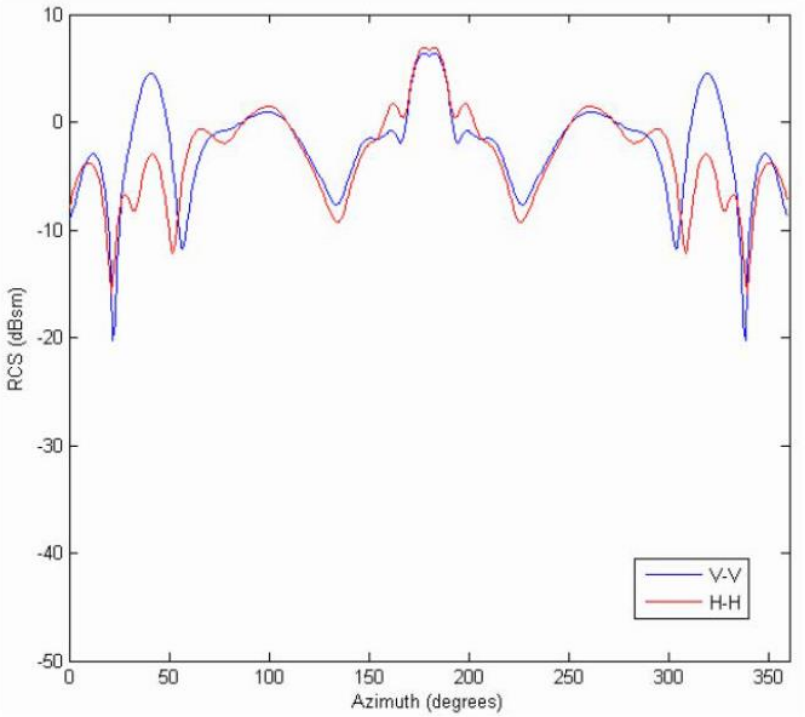

Figure 1. Monostatic RCS analysis of a standing human [3].

2.2.2 Orientation Angle

The amount of energy being backscattered towards the radar is greatly dependent on the orientation angle of the target relative to the transceiver. For the human body, the highest amount of return tends to come from the back due to its large surface area. The monostatic RCS response at this orientation angle behaves similar to that of a flat-plate. The frontal and side views produce returns that are similar but weaker than that of the back view. Figure 1 shows the monostatic RCS of a human with vertically-polarized signal transmission and reception (VV) and horizontally-polarized signal transmission and reception (HH) polarizations.

The 0 degree azimuth refers to the front view while the 180 degree azimuth refers to the back view. In general, the RCS plots are very similar, with VV RCS about 10 dB higher than the HH RCS at 40 degrees and 320 degrees. It is also seen that the RCS from the back view is about 16 dB higher than that observed from the front.

2.2.3 Breathing Effects

The effects respiration has on RCS measurements has been studied in many ways recently using a variety of radar systems [4]-[7]**.** Breathing will cause the amount of energy that is backscattered toward the radar to vary. This slight movement of a person's chest, namely expansion and contraction, will cause the RCS of that person to continuously be Doppler-modulated with each breath. In Refs. [8]-[9], the RCS of a human's breathing movements was measured. It should be noted that the RCS was not a measure of the chest or person but rather a measure of the breathing motion itself. The results showed a relatively linear correlation between frequency and RCS over a band ranging from 500 MHz to 2 GHz. The averaged data shows the RCS increasing from roughly -42 dBm^2 to -22 dBm^2 as a function of frequency [8], [9].

Further research was done that involved finding what the effective radar cross section (ERCS) due to breathing and heartbeat [6]. ERCS differs from the traditional RCS in that it involves only certain regions of a body and not the body as a whole. The ERCS studied in [10] corresponds to the parts of the human body that are in motion due to respiration and heartbeat, nothing else. The traditional RCS of a human will be much larger than the ERCS we are analyzing. This is because the RCS takes into all the other parts of the body (i.e. arms, legs, head, etc.). These other body parts are irrelevant to our research, though, because we are considering them to be motionless and, thus, register on a Doppler radar as static clutter. Rather,

we are focused on studying Doppler signatures from cardiopulmonary movements which will show up outside of the clutter region. So, it is important that our calibration target specifically resemble ERCS. The author's dissertation focused on finding these ERCS values and he did this by gathering data on human test subjects.

The body characteristics of the human test subjects were first analyzed before looking into their ERCS values. The goal of the analysis was to sort through the 20 participants and find two (1 male, 1 female) who best-resembled the "average" human. The basis for "average" was developed by analyzing data from the Centers for Disease Control and Prevention (CDC) via the U.S. Department of Health and Human Services [11]. The three statistics considered were height, weight, and body mass index (BMI). These data were gathered on adults 20+ years in age. Over ten thousand humans were polled. The average adult male had a height of 175.9 cm (or ~5'9"). For females, the average height was 162.1 cm (or ~5'4"). For weight, the average male and female adult was 88.7 kg and 75.4 kg, respectively. The average BMI indices for male and female adults were 28.6 and 28.7, respectively. Using this information, twenty test subjects in [10] were sorted through to find a male and female who most fit this description. Tables 1-3 below show this analysis. The second to last column represents the percent difference between the subject and the average for his/her particular age group (i.e. 20-29, 30-39, 40-49, etc.). The last column represents the percent difference between the subject and the average for all adult males or females 20+ years of age.

Table 1. An analysis on the heights of the human test subjects.

Number	Age	Gender	Height [cm]	Avg Ht by Age	% Diff	Abs % Diff by age group	Abs % Diff (20+)
1	30	M	164.5	176.4	-7%	6.7%	6.5%
2	33	M	174.0	176.4	-1%	1.4%	1.1%
3	45	M	172.0	176.8	-3%	2.7%	2.2%
4	42	F	172.7	163.1	6%	5.9%	6.5%
5	24	M	175.0	176.3	-1%	0.7%	0.5%
6	23	F	155.0	163.1	-5%	5.0%	4.4%
7	25	M	179.0	176.3	2%	1.5%	1.8%
8	31	M	177.8	176.4	1%	0.8%	1.1%
9	63	F	164.0	161.6	1%	1.5%	1.2%
10	22	M	171.0	176.3	-3%	3.0%	2.8%
11	41	F	164.0	163.1	1%	0.6%	1.2%
12	24	M	180.3	176.3	2%	2.3%	2.5%
13	26	M	186.0	176.3	6%	5.5%	5.7%
14	27	M	182.8	176.3	4%	3.7%	3.9%
15	75	F	162.0	159.1	2%	1.8%	0.1%
16	28	M	182.8	176.3	4%	3.7%	3.9%
17	33	F	178.0	163.4	9%	8.9%	9.8%
18	27	M	188.0	176.3	7%	6.6%	6.9%
19	35	M	185.0	176.4	5%	4.9%	5.2%
20	29	M	167.0	176.3	-5%	5.3%	5.1%

Table 2. An analysis on the weights of the human test subjects.

Number	Age	Gender	Weight [kg]	Avg Wt by Age	% Diff	Abs % Diff by age group	Abs % Diff (20+)
1	30	M	86.1	90.5	-5%	5%	2.9%
2	33	M	80.3	90.5	-11%	11%	9.5%
3	45	M	82.1	91.0	-10%	10%	7.4%
4	42	F	62.3	76.2	-18%	18%	17.4%
5	24	M	61.3	83.4	-26%	26%	30.9%
6	23	F	45.7	73.4	-38%	38%	39.4%
7	25	M	77.2	83.4	-7%	7%	13.0%
8	31	M	79.4	90.5	-12%	12%	10.5%
9	63	F	66.8	77.4	-14%	14%	11.4%
10	22	M	80.8	83.4	-3%	3%	8.9%
11	41	F	61.3	91.0	-33%	33%	18.7%
12	24	M	86.1	83.4	3%	3%	2.9%
13	26	M	87.5	83.4	5%	5%	1.4%
14	27	M	77.0	83.4	-8%	8%	13.2%
15	75	F	67.0	74.8	-10%	10%	11.1%
16	28	M	87.3	83.4	5%	5%	1.6%
17	33	F	84.8	76.7	11%	11%	12.5%
18	27	M	104.8	83.4	26%	26%	18.2%
19	35	M	75.6	90.5	-16%	16%	14.8%
20	29	M	70.1	83.4	-16%	16%	21.0%

Table 3. An analysis on the BMI indices of the human test subjects.

Number	Age	Gender	BMI [kg/m^2]	Avg BMI by Age	% Diff	Abs % Diff by age group	Abs % Diff (20+)
1	30	M	31.8	29	10%	10%	11.2%
2	33	M	26.5	29	-9%	9%	7.3%
3	45	M	27.8	29	-4%	4%	2.8%
4	42	F	20.9	28.6	-27%	27%	27.2%
5	24	M	20	26.8	-25%	25%	30.1%
6	23	F	19	27.5	-31%	31%	33.8%
7	25	M	24.1	26.8	-10%	10%	15.7%
8	31	M	25.1	29	-13%	13%	12.2%
9	63	F	24.8	29.6	-16%	16%	13.6%
10	22	M	27.6	26.8	3%	3%	3.5%
11	41	F	22.8	28.6	-20%	20%	20.6%
12	24	M	26.5	26.8	-1%	1%	7.3%
13	26	M	25.3	26.8	-6%	6%	11.5%
14	27	M	23	26.8	-14%	14%	19.6%
15	75	F	25.5	29.5	-14%	14%	11.1%
16	28	M	26.1	26.8	-3%	3%	8.7%
17	33	F	26.8	28.7	-7%	7%	6.6%
18	27	M	29.65	26.8	11%	11%	3.7%
19	35	M	22.1	29	-24%	24%	22.7%
20	29	M	25.1	26.8	-6%	6%	12.2%

Ideally, we would like to see as many green boxes as possible as this would indicate a small difference between the subject and the average values. After analyzing this data, two males and two females were chosen out of the bunch which were believed to best represent the average adult male and female. These test subjects were numbers 10, 12, 15, and 17. Table 4 shows various data on these subjects. As we can see, the ERCS is fairly small compared to the traditional RCS value of the entire human body (~1 m^2).

Table 4. Data from test subjects who best-represented the average male and female adult.

Number	Age	Gender	Height [cm]	Weight [kg]	BMI [kg/m^2]	Supine RCS (sm)	Sphere Diameter (inches)	Prone RCS (sm)	Sphere Diameter (inches)	Side RCS (sm)	Sphere Diameter (inches)
10	22	M	171	80.8	27.6	0.003	**2.4**	0.045	**9.4**	0.002	**2.0**
12	24	M	180.3	86.1	26.5	n/a	**n/a**	0.249	**22.2**	0.003	**2.5**
15	75	F	162.0	67.0	25.5	0.03	**7.7**	0.008	**4.1**	0.0003	**0.7**
17	33	F	178	84.8	26.8	0.112	**14.9**	0.018	**6.0**	0.013	**5.0**

One particular observation is that the ERCS, when taken from the side of a human, will be very small. This is logical because the region of the body moving, when viewed from the side, has a small surface area. Using this information, we decided to base our calibration target off of participant number 12. We felt as if this ERCS was a good measure of the average person.

3. The Sphere as a Calibration Device

2.3.1 Background

The PEC sphere is an essential tool in radar-related testing due to its RCS reliability. The geometry of a sphere naturally possesses a unique quality in that its RCS is angularly independent of the source's location. In other words, an observer, whose radial distance stays constant with the target, will see the same backscatter at all observation angles around the sphere. The backscattered power for other common objects (e.g. flat plate, corner reflector) heavily fluctuates depending on the source's incident angle. For this reason, calibration is rather difficult with the aforementioned objects as even the slightest miscalculation in incident angle can corrupt the calibration process. Because of the sphere's angular independence, accurate calibration can be achieved by simply knowing only the distance between the source and target. Due to the sphere's common usage in calibration, there are well-detailed analytical solutions that derive the RCS of this geometry; something of utter importance to assure proper calibration.

2.3.2 Theory

This section borrows derivations from pp. 655-663 in [2]. To attain the RCS of a PEC sphere, we first assume an incident, uniform plane wave is traveling along the z-axis and polarized along the x-axis. In spherical coordinates, the wave's electric field will be represented as

$$\mathbf{E}^i = \hat{\mathbf{a}}_x E_x^i = \hat{\mathbf{a}}_x E_0 e^{-j\beta z} = \hat{\mathbf{a}}_\mathbf{x} E_0 e^{-j\beta r\cos\theta} \tag{2.2}$$

Using the following transformation between Cartesian and spherical components,

$$A_x = A_r \sin\theta\cos\phi + A_\theta \cos\theta\cos\phi - A_\phi \sin\phi \tag{2.3}$$

the incident electric field can be represented as

$$\mathbf{E}^i = \hat{\mathbf{a}}_r E_r^i + \hat{\mathbf{a}}_\theta E_\theta^i + \hat{\mathbf{a}}_\phi E_\phi^i \tag{2.4}$$

where the spherical components of the electric field are

$$E_r^i = E_0 \frac{\cos\phi}{j\beta r}\frac{\partial}{\partial\theta}\left(e^{-j\beta r\cos\theta}\right) \tag{2.5}$$

$$E_\theta^i = E_0 \cos\theta\cos\phi\, e^{-j\beta r\cos\theta} \tag{2.6}$$

$$E_\phi^i = -E_0 \sin\phi\, e^{-j\beta r\cos\theta} \tag{2.7}$$

These components can be expressed via spherical Bessel functions and Legendre functions of the first kind. Further modification of these components, yields

$$E_r^i = -jE_0 \frac{\cos\phi}{(\beta r)^2} \sum_{n=1}^{\infty} j^{-n}(2n+1)\hat{J}_n(\beta r)P_n^1(\cos\theta) \tag{2.8}$$

$$E_\theta^i = E_0 \frac{\cos\theta\cos\phi}{\beta r} \sum_{n=0}^{\infty} j^{-n}(2n+1)\hat{J}_n(\beta r)P_n^0(\cos\theta) \tag{2.9}$$

$$E_\phi^i = -E_0 \frac{\sin\phi}{\beta r} \sum_{n=0}^{\infty} j^{-n}(2n+1)\hat{J}_n(\beta r)P_n^0(\cos\theta) \tag{2.10}$$

where $\hat{J}_n$ is a spherical Bessel function of the first kind. To relate the incident fields with the scattered fields, in route to solving for RCS, it is convenient to express both as a superposition of transverse electric (TE) and transverse magnetic (TM) fields. To solve for the TE fields, we must establish two vector potentials for the incident fields, **A** and **F**, where **A** = 0 and **F** = $\hat{\mathbf{a}}_r F_r(r,\theta,\phi)$. $F_r(r,\theta,\phi)$ is a solution to the scalar Helmholtz equation in spherical coordinates. A similar approach is used to find incident TM fields, with **A** = $\hat{\mathbf{a}}_r A_r(r,\theta,\phi)$ and **F** = 0. By expressing the incident radial electric field in terms of TM^r, the following relationship is formed.

$$E_r^i = \frac{1}{j\omega\mu\varepsilon}\left(\frac{\partial^2}{\partial r^2} + \beta^2\right)A_r^i \tag{2.11}$$

A_r^i can then be found by equating (2.11) to (2.8) which results in

$$A_r^i = E_0 \frac{\cos\phi}{\omega} \sum_{n=1}^{\infty} a_n \hat{J}_n(\beta r)P_n^1(\cos\theta) \tag{2.12}$$

with

$$a_n = j^{-n}\frac{(2n+1)}{n(n+1)} \tag{2.13}$$

This equation is very valuable in that it can then be plugged back into (2.11) to find the incident radial electrical at the sphere.

To find the incident radial magnetic field, it is put in terms TE^r fields and the same approach is taken using the reversed vector potentials (**A** = 0 and **F** = $\hat{\mathbf{a}}_r F_r(r,\theta,\phi)$). The resulting **F** vector potential in the radial direction becomes

$$F_r^i = E_0\frac{\sin\phi}{\omega\eta}\sum_{n=1}^{\infty} a_n \hat{J}_n(\beta r)P_n^1(\cos\theta) \tag{2.14}$$

From this, the incident magnetic field at the surface of the sphere can be calculated by plugging this equation into

$$H_r^i = \frac{1}{j\omega\mu\varepsilon}\left(\frac{\partial^2}{\partial r^2}+\beta^2\right)F_r^i \tag{2.15}$$

As stated above, equations (2.12) and (2.14) allow for the incident electric and magnetic fields to be calculated, and with this information all of the other incident electric and magnetic field components can be found. The scattered fields can be found in the same manner using slightly different vector potentials **A** and **F**. These modified vector potentials add coefficients, b_n and c_n, that account for boundary conditions at the surface of the sphere. This modification also replaces the spherical Bessel functions used in the incident vector potentials with spherical Hankel functions of the second kind, $\hat{H}_n^{(2)}(\beta r)$, to signify outward traveling waves moving away from the sphere upon reflection. Using superposition on the incident and scattered fields, two

new vector potentials, A_r^t and F_r^t, are defined to represent the total radial field. They are defined as

$$A_r^t = A_r^i + A_r^s = E_0 \frac{\cos\phi}{\omega} \sum_{n=1}^{\infty} \left[a_n \hat{J}_n(\beta r) + b_n \hat{H}_n^{(2)}(\beta r) \right] P_n^1(\cos\theta) \tag{2.16}$$

$$F_r^t = F_r^i + F_r^s = E_0 \frac{\sin\phi}{\omega\eta} \sum_{n-1}^{\infty} \left[a_n \hat{J}_n(\beta r) + c_n \hat{H}_n^{(2)}(\beta r) \right] P_n^1(\cos\theta) \tag{2.17}$$

The boundary condition coefficients are found by setting E_θ^t and E_ϕ^t to zero at the boundary. This leads to

$$b_n = -a_n \frac{\hat{J}_n'(\beta a)}{\hat{H}_n^{(2)\prime}(\beta a)} \tag{2.18}$$

$$c_n = -a_n \frac{\hat{J}_n(\beta a)}{\hat{H}_n^{(2)}(\beta a)} \tag{2.19}$$

where $' = \frac{\partial}{\partial(\beta r)}$ for the Bessel and Hankel functions. Using these coefficients, the vector potentials in (2.16) and (2.17) can be completed and scattered electric field components are as follows.

$$E_r^s = -jE_0 \cos\theta \sum_{n=1}^{\infty} b_n \left[\hat{H}_n^{(2)''}(\beta r) + \hat{H}_n^{(2)}(\beta r) \right] P_n^1(\cos\theta) \tag{2.20}$$

$$E_\theta^s = \frac{E_0}{\beta r} \cos\phi \sum_{n=0}^{\infty} \left[j b_n \hat{H}_n^{(2)\prime}(\beta r) \sin\theta \, P_n'^1(\cos\theta) - c_n \hat{H}_n^{(2)}(\beta r) \frac{P_n^1(\cos\theta)}{\sin\theta} \right] \tag{2.21}$$

$$E_\phi^s = \frac{E_0}{\beta r} \sin\phi \sum_{n=0}^{\infty} \left[j b_n \hat{H}_n^{(2)\prime}(\beta r) \frac{P_n^1(\cos\theta)}{\sin\theta} - c_n \hat{H}_n^{(2)}(\beta r) \sin\theta P_n'^1(\cos\theta) \right] \tag{2.22}$$

where $'' = \frac{\partial^2}{\partial(\beta r)^2}$ for the Hankel functions and $' = \frac{\partial}{\partial(\cos\theta)}$ for the Legendre functions. As βr grows larger, far field approximations can be used to simply (2.20) – (2.22). Under these approximations, the scattered, radial electric field will diverge to zero. With knowledge of both the incident and scattered fields, the bistatic and monostatic RCS equations for a PEC sphere can be found. Using (2.2) and (2.20) – (2.22), these two important parameters are defined as

$$\sigma(\text{bistatic}) = \frac{\lambda^2}{\pi}\left[\cos^2\phi|A_\theta|^2 + \sin^2\phi\left|A_\phi\right|^2\right] \tag{2.23}$$

$$\sigma(\text{monostatic}) = \frac{\lambda^2}{4\pi}\left|\sum_{n=1}^{\infty}\frac{(-1)^n(2n+1)}{\widehat{H}_n^{(2)'}(\beta r)\widehat{H}_n^{(2)}(\beta r)}\right|^2 \tag{2.24}$$

where

$$|A_\theta|^2 = \left|\sum_{n=1}^{\infty} j^n\left[b_n \sin\theta\, P_n'^1(\cos\theta) - c_n\frac{P_n^1(\cos\theta)}{\sin\theta}\right]\right|^2 \tag{2.25}$$

$$\left|A_\phi\right|^2 = \left|\sum_{n=1}^{\infty} j^n\left[b_n\frac{P_n^1(\cos\theta)}{\sin\theta} - c_n \sin\theta\, P_n'^1(\cos\theta)\right]\right|^2 \tag{2.26}$$

A plot of (2.24) is shown in Figure 2 as a function of radius [2]. Depending on the wavelength of the signal, some useful approximations can used during the calibration process to estimate monostatic RCS. If the radius of the calibration sphere is less than 0.1λ, it operates in the Rayleigh region. In this region, (2.22) reduces to

$$\sigma(\text{monostatic}) = \frac{9\lambda^2}{4\pi}(\beta r) \tag{2.27}$$

Although the proposed calibration target is not frequency independent, a known RCS can be calculated based off of only a few parameters. A sphere whose radius is more than twice the wavelength ($r > 2\lambda$), operates in the approximating area known as the optical region. In this region, the monostatic RCS of the sphere is equivalent to πr^2, the area of a circle. This region is very favorable for calibration; the RCS is dependent on just one factor, the sphere's radius. All other parameters (i.e. frequency, aspect angle) become irrelevant. The equations derived in this section show the natural, advantageous RCS properties a PEC sphere possesses. It is because of these properties that we decided to construct our target with spherical-like architecture. Ideally, our target would appear to the radar exactly as a smooth sphere would. To add a dynamic element to our design, however, there will be some tradeoffs.

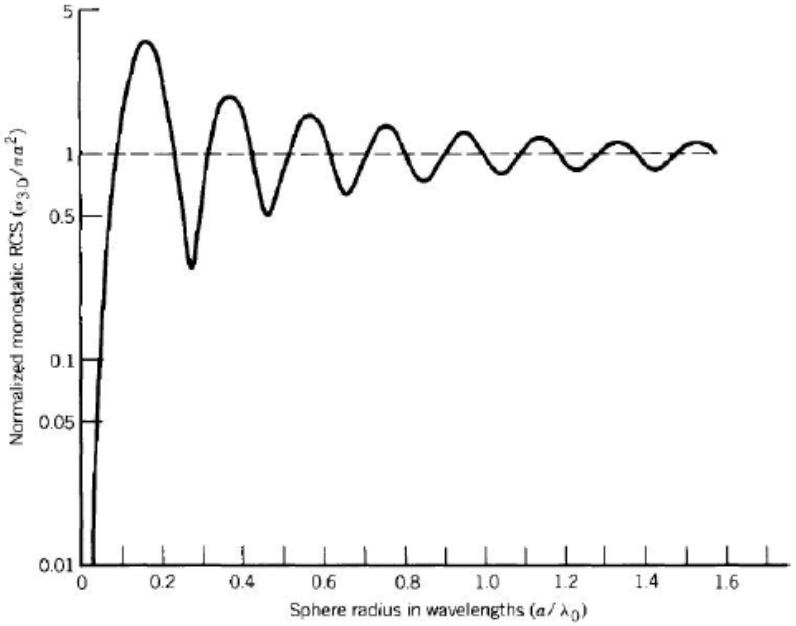

Figure 2. Normalized monostatic RCS of a sphere as a function of radius [2].

4. Emulating Human RCS

As stated in the previous section, spherical geometries possess very advantageous qualities in regards to calibration. For this reason, we decided to model our design with a spherical geometry. Assuming operation in the optical region, a human torso ERCS value of 0.2 m^2 can be obtained using a sphere of radius 25 cm. Furthermore, from Figure 2, we note that the optical region starts approximately when the radius to wavelength ratio is about 1.6. Thus, to be in the optical region, the wavelength must be less than 25 ÷ 1.6 = 15.6 cm, or the frequency must be higher than 1.9 GHz.

We were faced with a unique challenge, though, in that our spherical design had to possess the ability to expand and contract radially for future Doppler applications. One of the methods for doing this is an air compression system that inflates and deflates the target like a balloon. However, this is insufficient for our situation because future applications will require a robust structure somewhat mobile and capable of being buried under rubble; we felt as if a stronger design was needed.

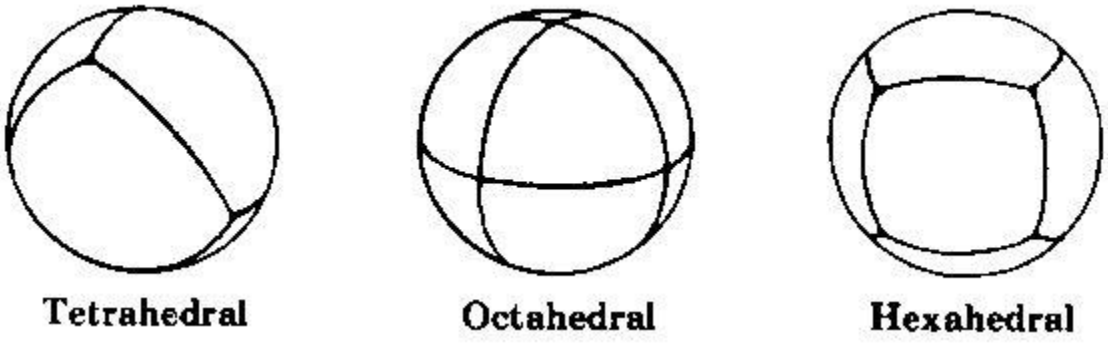

Figure 3. Three different types of spherical polyhedra.

We landed on the idea of creating a structure whose geometry resembles a spherical polyhedral. This is essentially a perfect sphere divided into *n* number of faces. Figure 3 shows three different types of spherical polyhedra. Segmenting the sphere in such ways opens up the possibility for simultaneous expansion and contraction of the device as a whole. It is envisioned that the center of each face will be connected to internal mechanics which, in turn, force the faces to oscillate radially back and forth, thus mimicking respiration.

The major issue with this approach is in regards to the gaps that form between the faces when each piece expands. Though the expansion may be on the scale of millimeters, these gaps will introduce electrical discontinuities to our design and could take away the advantageous qualities our continuous sphere possesses. To analyze this effect, we simulated various spherical geometries. The end goal was to find a geometry that best-maintained sphere-like calibration qualities (e.g. aspect independence) whilst in the expanded state.

Chapter 3 – Simulation Process

1. Parameters

The five geometries simulated were the tetrahedron (4 faces), hexahedron (6 faces), octahedron (8 faces), dodecahedron (12 faces), and icosahedron (20 faces). Each device was to be 50 cm in diameter with a plate thickness of 2 mm. For the target in its expanded state, each plate was radially displaced 10 mm. This can be thought of as the maximum displacement a human's torso would move during respiration. In the target's contracted state, we displaced each face 0.2 mm. This small expansion was used to implement the electrical discontinuities that still exist in the contracted state due to each face being its own separate piece. RCS simulations were compiled at 3.6 GHz for each geometry in each of the two states; resulting in ten simulations. Vertical polarization was used at both the transmitting and receiving end (V/V). In both the contracted and expanded state, the target is operating in the optical region. Using the far field approximation discussed in section 2.3.2, the theoretical RCS for the contracted target is 0.196 m^2 (−7.07 dBm^2). In the target's expanded state, the theoretical RCS is 0.204 m^2 (−6.90 dBm^2). Again, these calculations assume a perfect sphere; the electrical discontinuities in our target may cause different results.

2. Creating the Models

Constructive Solid Geometry (CSG) is a popular method for generating complex solids in computing. The simulation models were generated using CSG techniques. This method functions by finding polygonal boundaries among two solids and performing Boolean operations at the boundary points [12]. Spherical polyhedra were generated by circumscribing a polyhedron inside a sphere. The intersection points between the polyhedron and the sphere define the vertices for each face of the calibration model (thus defining a spherical polyhedron). Once the vertices for the faces of the calibration model are established, the polyhedron inside the sphere is deleted. After this step, all that remains is the spherical polyhedron that is to be used as the simulation model.

If the sphere is a bit larger and does not exactly circumscribe the polyhedron, processing is done to project the intersection points from the vertices of the polyhedron to the surface of the sphere. Once these vertices are defined on the sphere, the same process, as mentioned above, is performed to form the model. This technique allows for spherical polyhedra to be generated that have small gaps in between their faces.

3. Results

The simulations were performed using a physical optics (PO) solver in FEKO, a computational electromagnetic software. The results are shown graphically in a three-dimensional format. The most important characteristic we are looking for in these results is aspect independence. Ideally, a geometry will possess a constant RCS over its entire surface

even in whilst expanded. The five geometries are shown in Figures 4-8. The results for each geometry are grouped together at the end of the chapter in Figures 9-18.

The first geometry shown is the 4-sided tetrahedron in Figure 4. The monostatic RCS results are given in Figures 9 and 10 for the contracted and expanded positions, respectively. In the contracted state, the target's RCS appears constant over the entirety of the surface. The simulation results show an RCS of approximately 0.20 m^2 which is consistent with the theoretical approximation. As expected, much of the RCS consistency is lost in the expanded state due to the gaps that come about. It is in our estimation that the higher RCS levels are likely due to plane waves traveling between the gaps, reflecting off of the inside, and interfering constructively on the path back towards the radar. These bright spots on the target could have an unwanted impact on data collection done using a tetrahedron geometry.

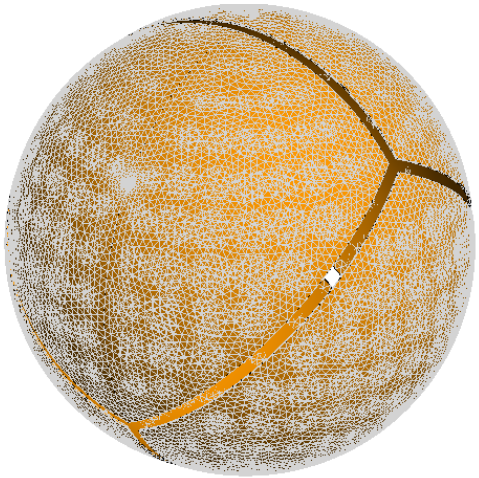

Figure 4. Tetrahedron geometry.

The second geometry shown is the 6-sided hexahedron shown in Figure 5. The monostatic RCS results are given in Figures 11 and 12 for the contracted and expanded positions, respectively. Again, there is great RCS consistency in the contracted state with numbers close to that of the theoretical approximation. The expanded state shows much less consistency in RCS, but the variance is not too high. For example, most of the variance in RCS is between 0.175 m^2 and 0.260 m^2. Though this is not ideal, it is encouraging that the range in RCS values (i.e. variance) are mostly within a small window. Unfortunately, higher RCS values in approaching 0.35 m^2 are once again seen in small areas on the sphere; concentrated mostly in towards the center of the face.

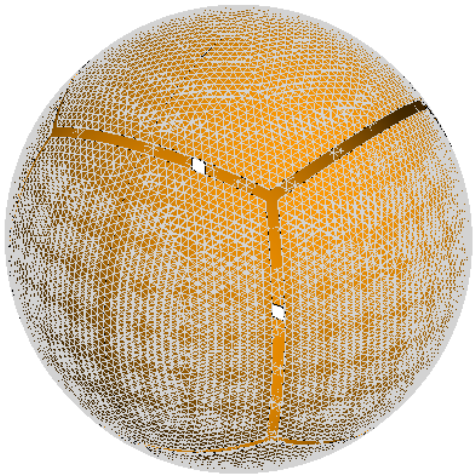

Figure 5. Hexahedron geometry.

The octahedron geometry is shown in Figure 6. Once again, the RCS remains very consistent when the target is in its contracted state. The octahedron also shows better RCS consistency in its expanded state than the tetrahedron and hexahedron. The variance in RCS is small similar to that of the hexahedron. Though there are a few high-RCS values that exist

towards the center of the faces, they appear to be a smaller quantity compared to the hexahedron.

Figure 6. Octahedron geometry.

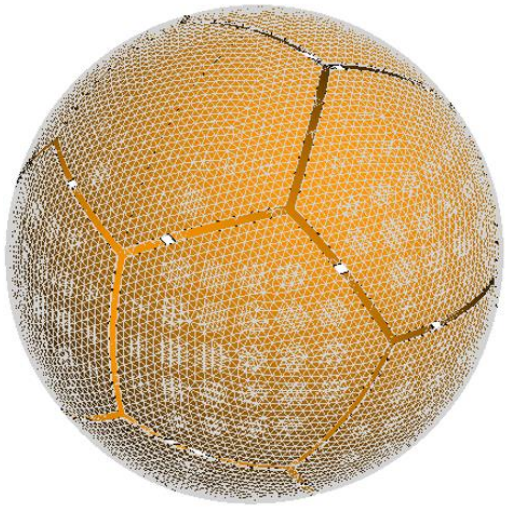

Figure 7. Dodecahedron geometry.

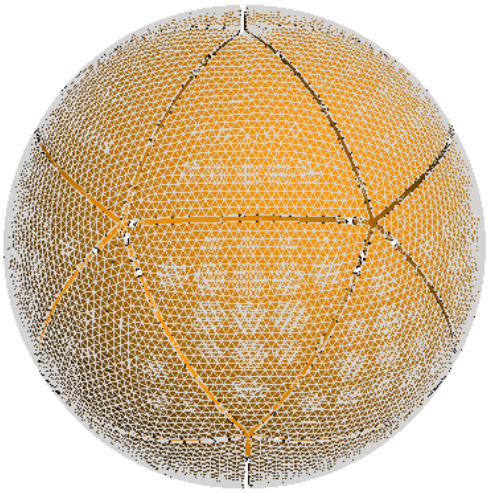

Figure 8. Icosahedron geometry.

The final two geometries are the 12-sided dodecahedron (Figure 7) and the 20-sided icosahedron (Figure 8). The monostatic RCS results for the dodecahedron are given in Figures 15 and 16 for the contracted and expanded positions, respectively. The dodecahedron possesses great RCS consistency while contracted, but a large amount of inconsistency when expanded. A clear pattern can be seen where bright spots exist at the center of each pentagonal face as well as at intersections where three faces intersect. Figures 17 and 18 show the monostatic RCS results for icosahedron in its contracted and expanded states, respectively. Like all of the other geometries, the icosahedron shows excellent RCS consistency over the entirety of its surface in the contracted state. In the expanded state, there are high levels of inconsistency likely due to the high number of discontinuities.

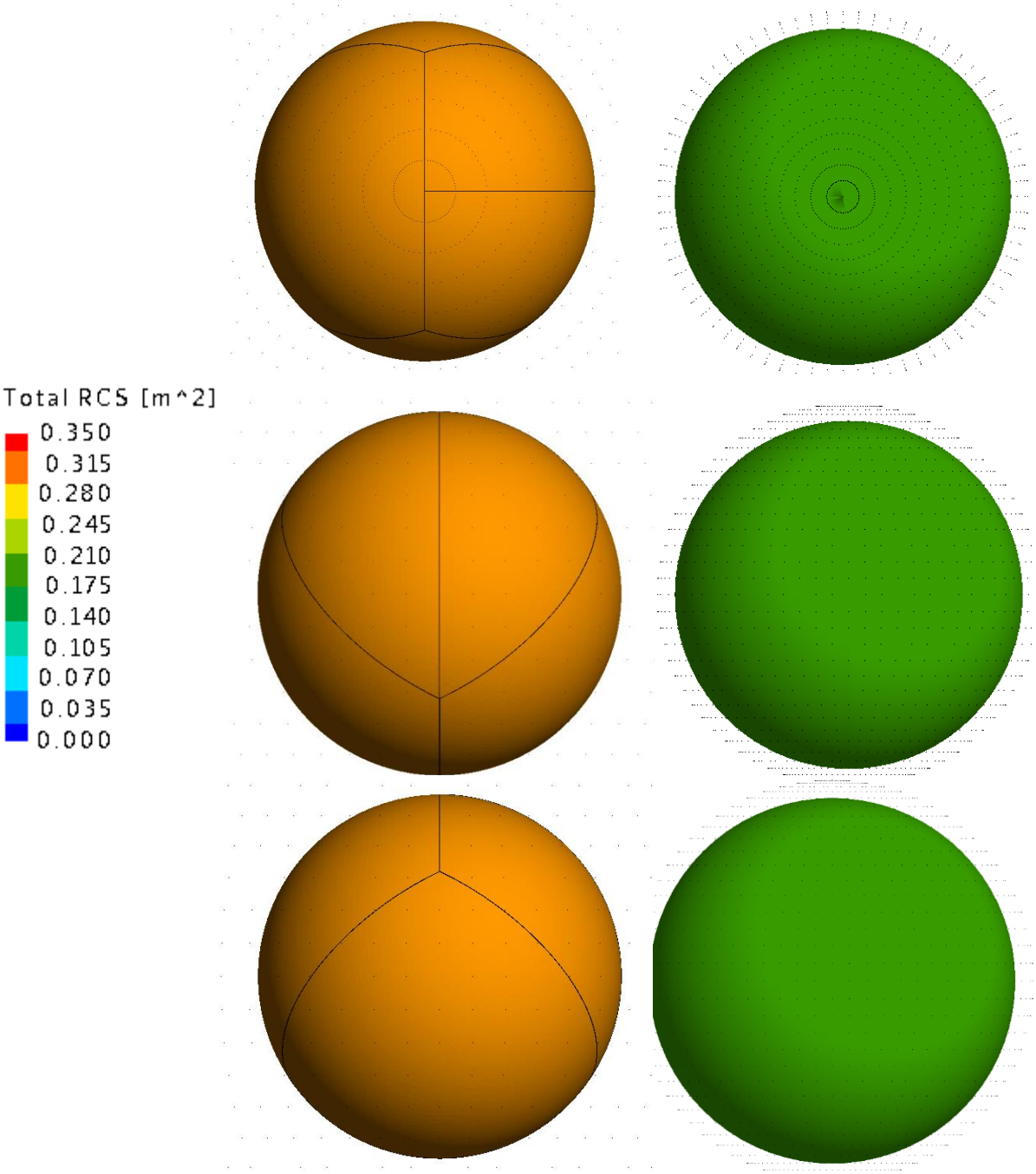

Figure 9. Monostatic RCS results for the contracted tetrahedron at 3.6 GHz.

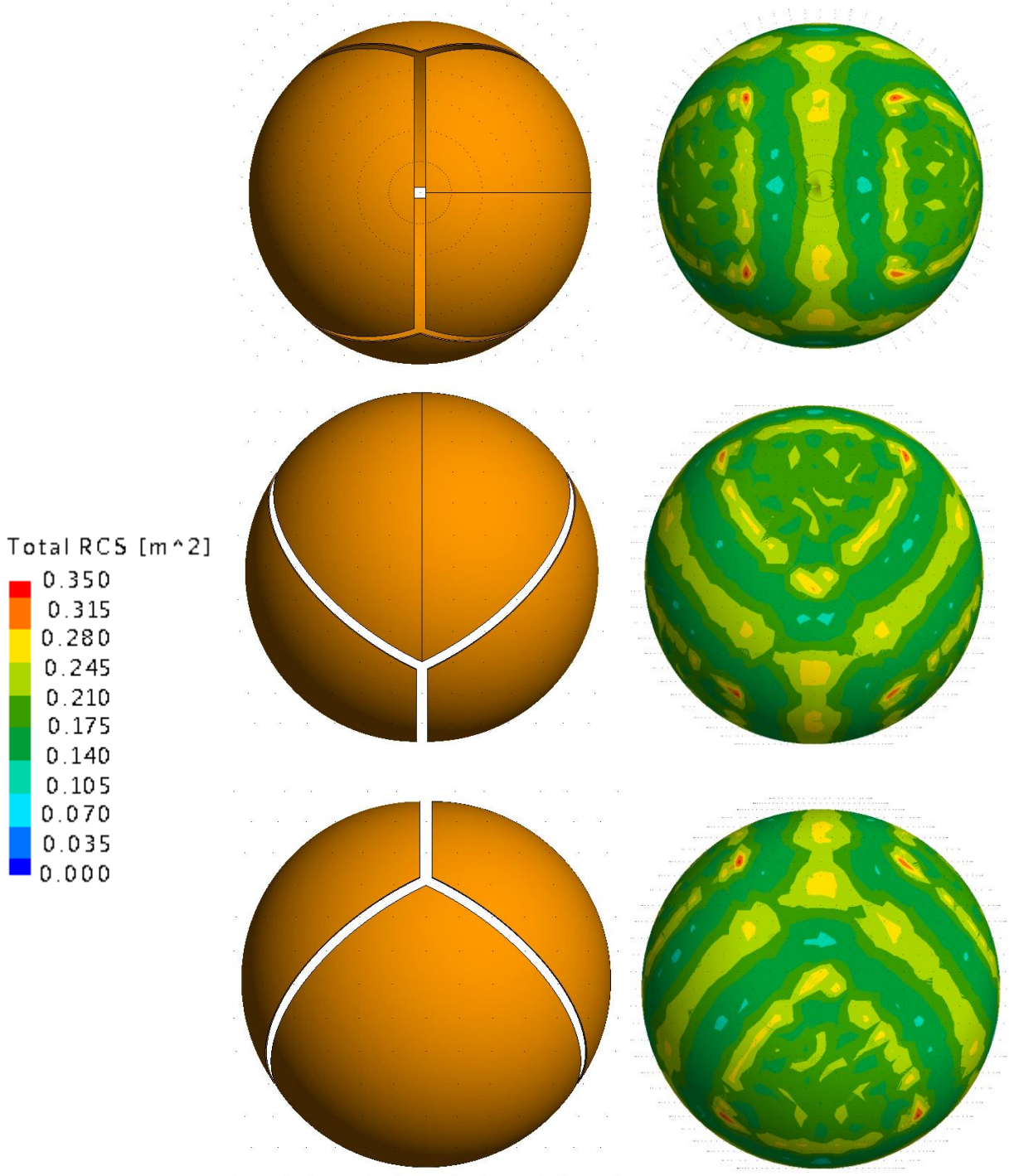

Figure 10. Monostatic RCS results for the expanded tetrahedron at 3.6 GHz.

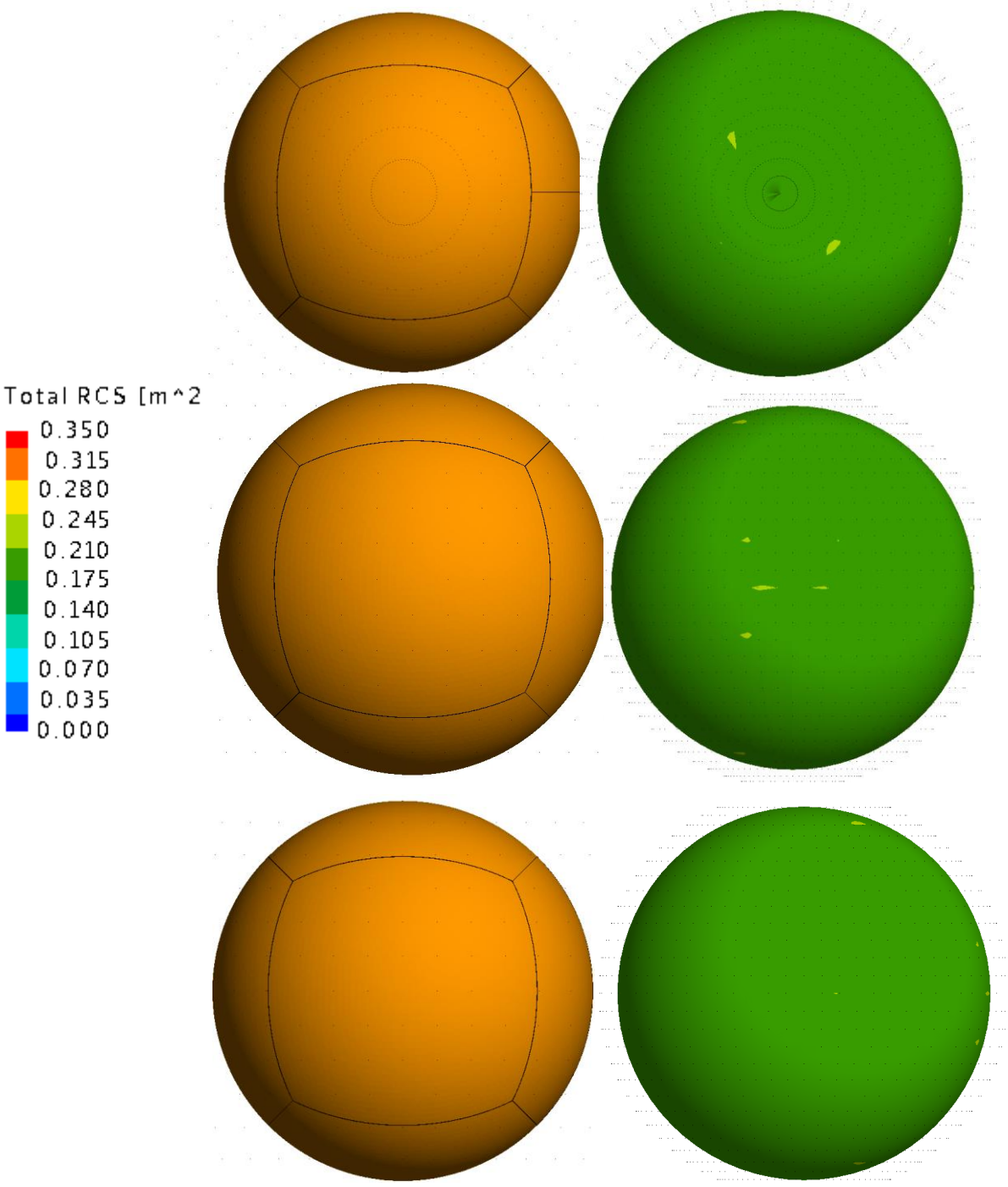

Figure 11. Monostatic RCS results for the contracted hexahedron at 3.6 GHz.

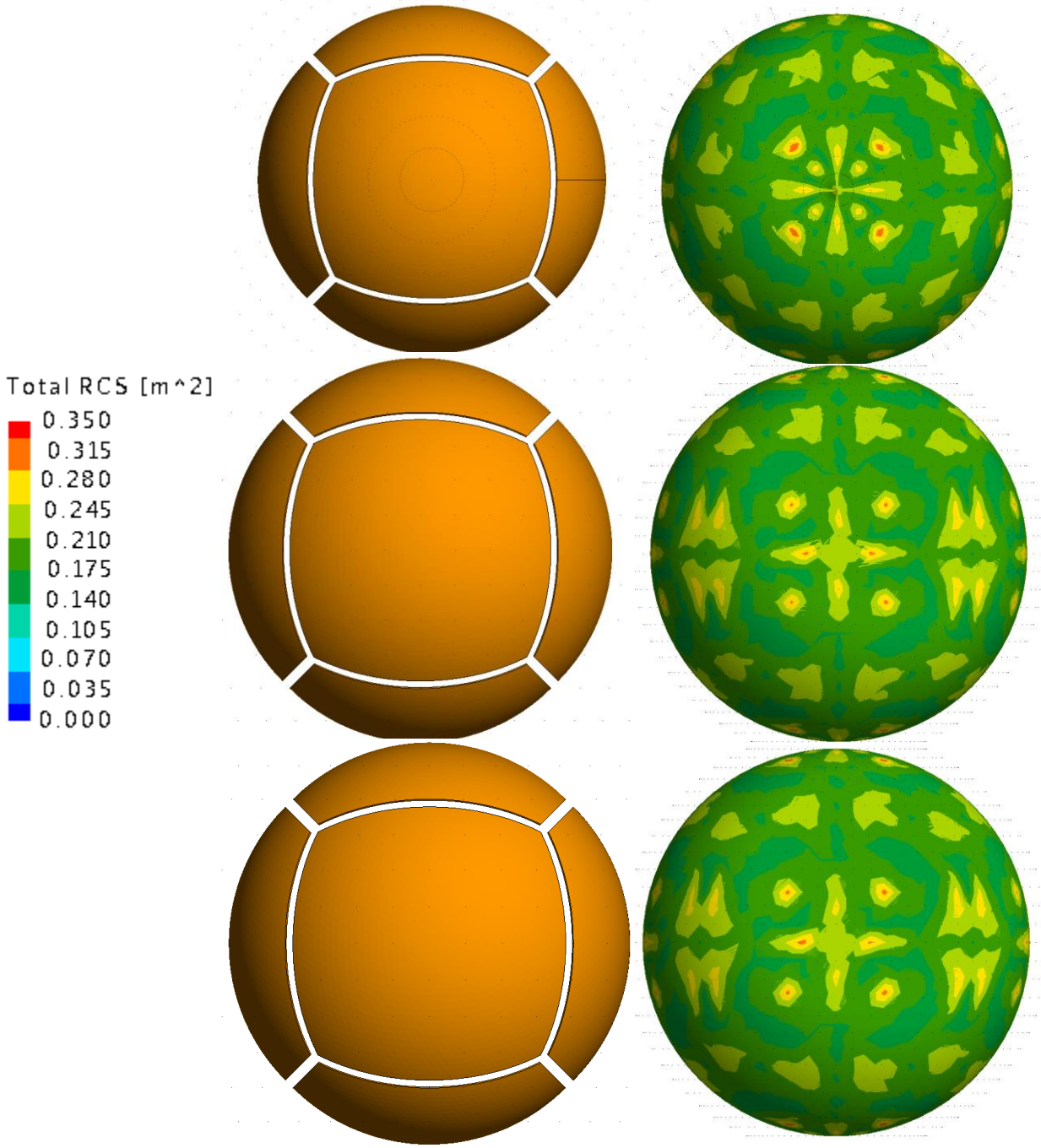

Figure 12. Monostatic RCS results for the expanded hexahedron at 3.6 GHz.

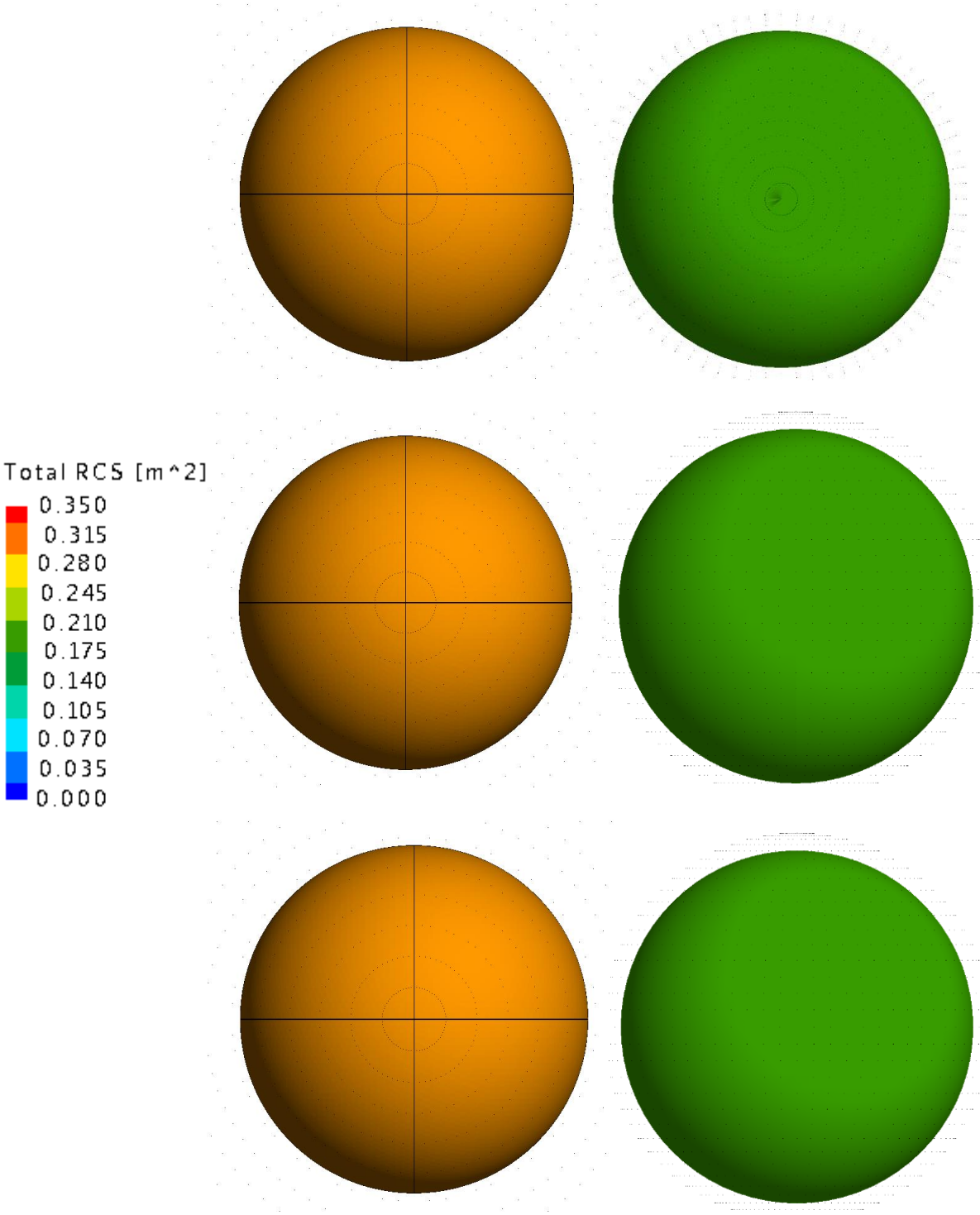

Figure 13. Monostatic RCS results for the contracted octahedron at 3.6 GHz.

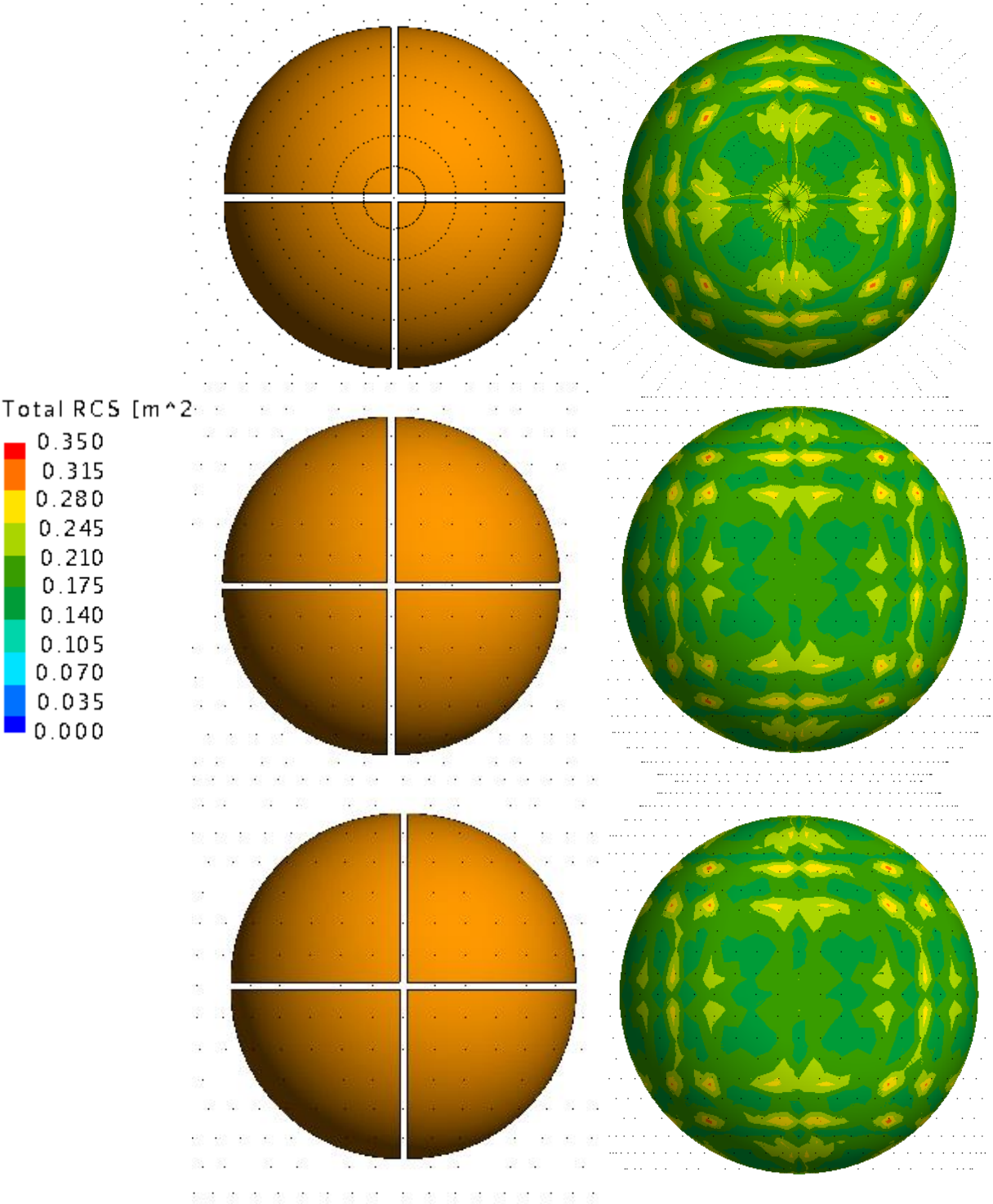

Figure 14. Monostatic RCS results for the expanded octahedron at 3.6 GHz.

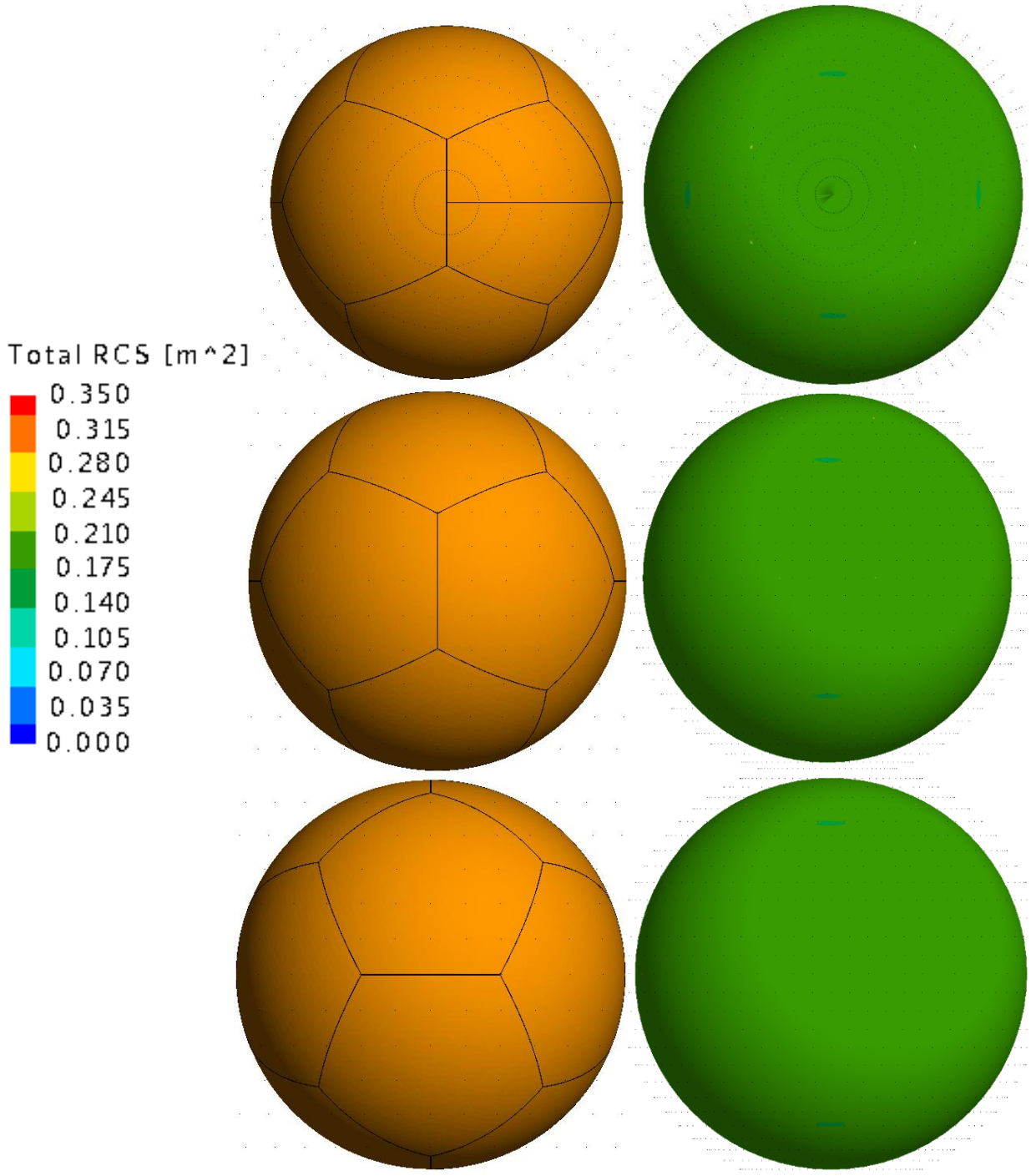

Figure 15. Monostatic RCS results for the contracted dodecahedron at 3.6 GHz.

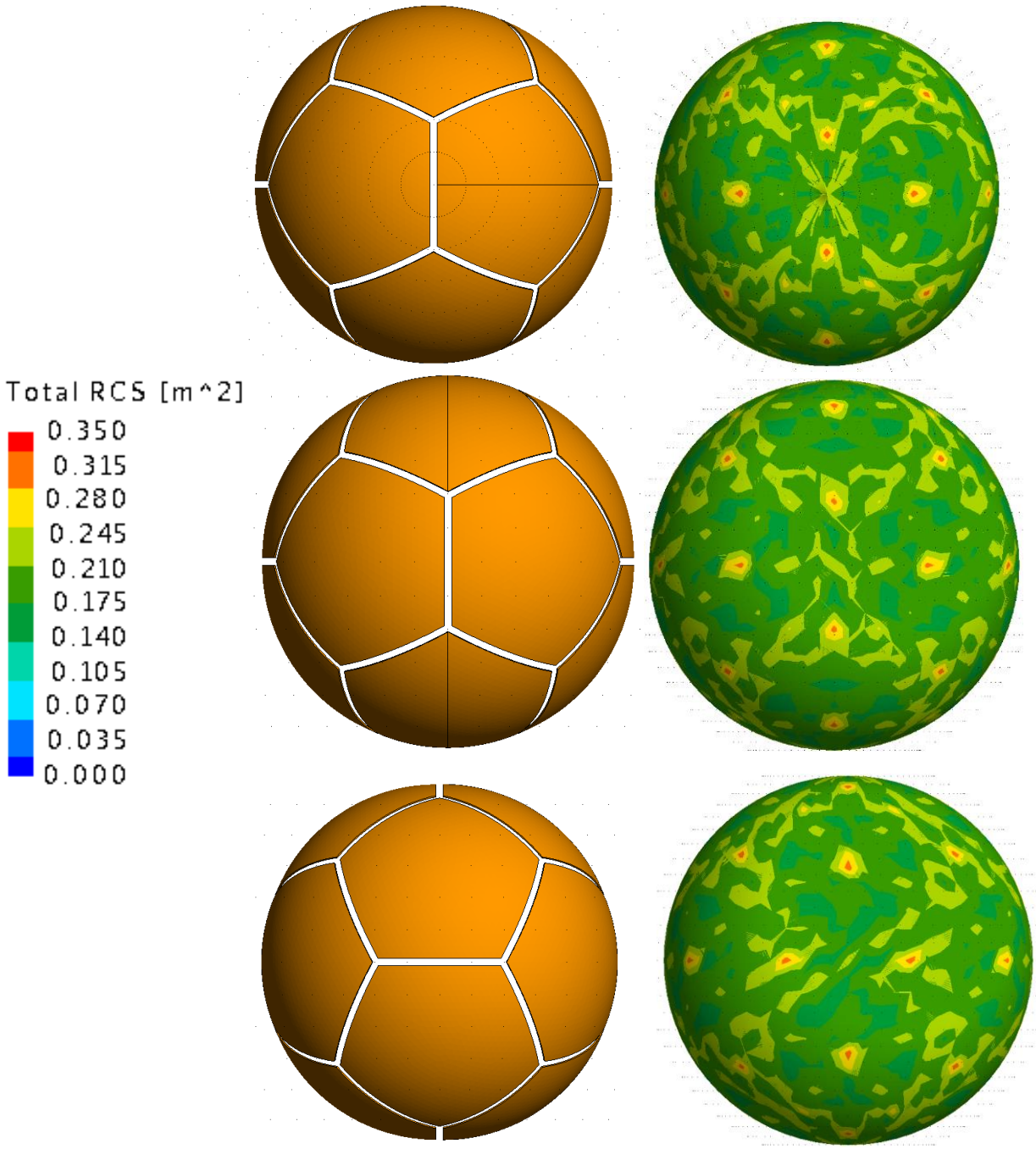

Figure 16. Monostatic RCS results for the expanded dodecahedron at 3.6 GHz.

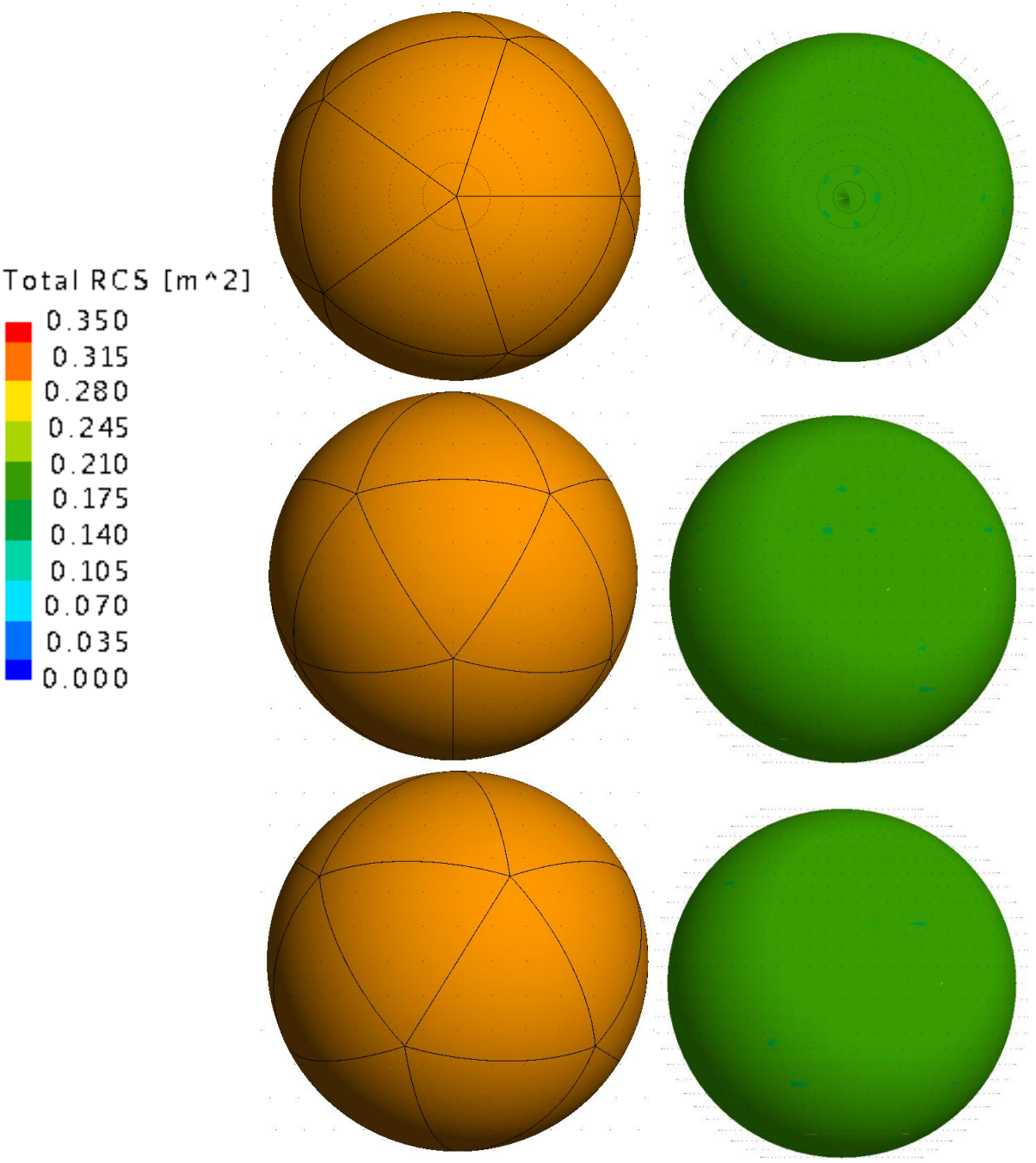

Figure 17. Monostatic RCS results for the contracted icosahedron at 3.6 GHz.

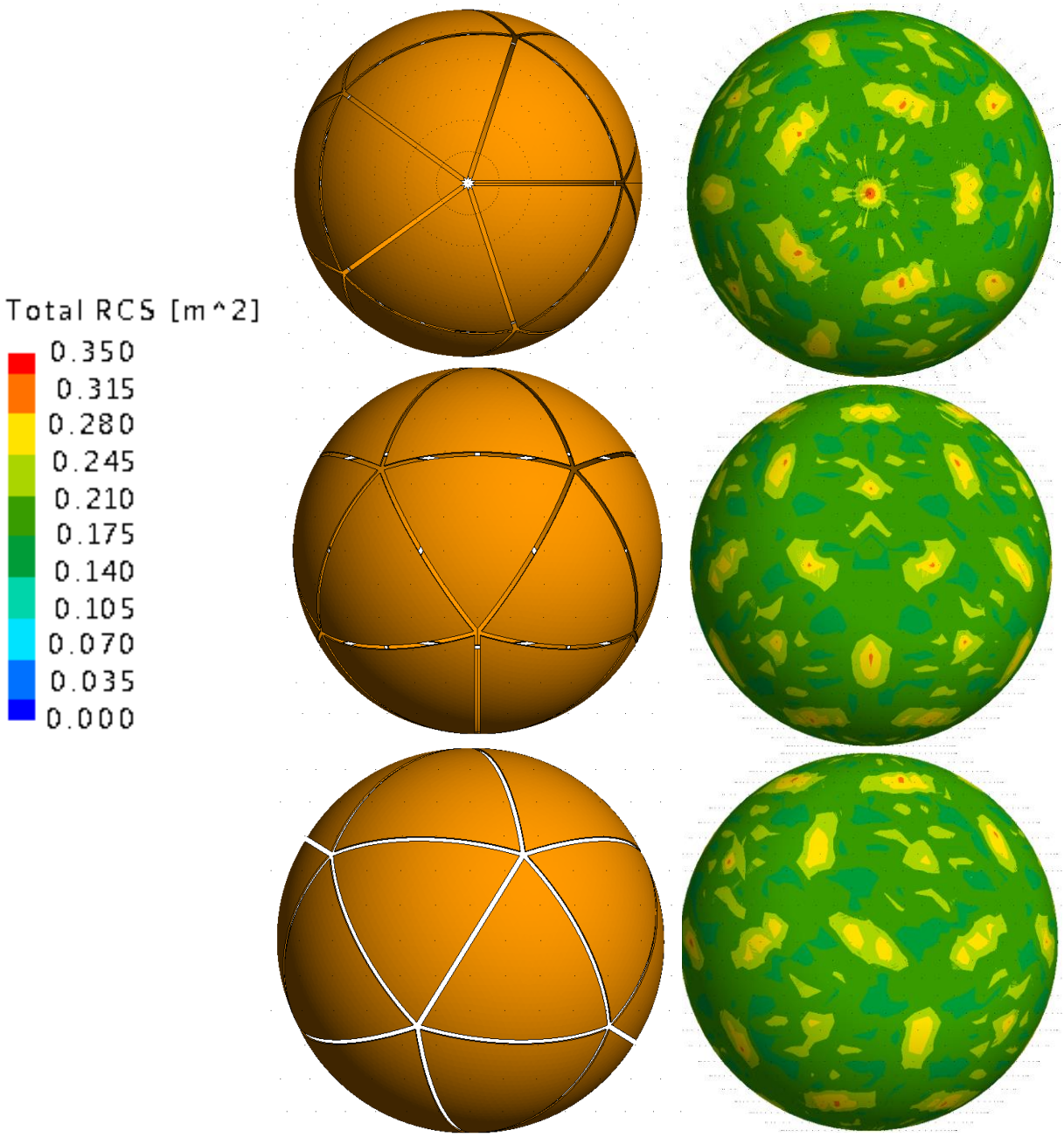

Figure 18. Monostatic RCS results for the expanded icosahedron at 3.6 GHz.

There are some common patterns and observations that can be taken away when analyzing the simulation results. The first is that our target performs exceptionally well in the contracted state for all geometries. Though we have small electrical discontinuities between faces, they are not great enough to prevent a very fine RCS consistency across the surfaces of the targets. Another observation is that the RCS tends to be higher at the gaps when in the expanded state. As mentioned earlier, a possible reason for this occurrence could be constructive interference happening when energy slips through the gaps and reflects in the specular direction back towards the radar whilst combining with energy reflected off of the surface of the target. Fortunately, the change in RCS is mild at approximately 17%, and may be considered insignificant depending on the application. A third observation is that the majority of bright spots on the targets occur in the center of the faces. Though it is unclear exactly why this happens, it can be hypothesized that the spots occur because these locations are the furthest away from the air gaps.

Of the five geometries simulated, the octahedron was chosen to be used for our target moving forward. The decision was based on the following factors: scattering profile, build complexity, and spherical projection. The scattering profile is completely based on the data gathered from the simulations. More specifically, the monostatic RCS profile. We felt as if the hexahedron and octahedron were the best two in this category because they showed the most RCS consistency in the expanded state. Moving on to build complexity, both the hexahedron and octahedron passed this criteria. Of the five geometries, the dodecahedron and icosahedron were clearly the hardest to build and their scattering profiles were not worth the attempt. In the future, the internal mechanics of this design will consist of linear actuators for each face and a control system to move each face simultaneously. It is important that the number of faces be

kept reasonably low not only due to build complexity but costs as well. The last category, spherical projection, is in regards to how well the target keeps its spherical shell in the expanded state. For example, the tetrahedron is very poor at this because it possesses just four faces. When the four faces move radially, large areas in the gaps of the target are formed without a velocity vector towards the radar. This is in contrast to the icosahedron target, where there are twenty faces moving radially and, thus, very few areas without a velocity vector moving towards the radar. These velocity vectors are very critical for performing Doppler measurements. This criteria was the deciding factor; we felt that having eight faces instead of six would be more efficient for Doppler testing in the future.

Chapter 4 – Prototype

1. Overview

A prototype was constructed to validate the simulation results presented in the previous section. The prototype forms an octahedron geometry capable of two states: full contraction and full radial expansion to 10 mm. RCS data are gathered and the scattering profile of the object is analyzed. The prototype is fully static.

2. Design

A fully-constructed CAD model of the prototype is shown in Figure 19. The model was generated using SolidWorks and maintains all of the dimensions used in the simulation model. The faces of the octahedron are all separate parts (eight total). The face piece is shown in Figure 20. The face pieces have a thickness of 2 mm. A holed connector piece is mounted directly on the center of the inside face. This is designed so that one end of a 1.905 cm (0.75 inch) dowel rod can be tightly inserted, thus forming an arm on the piece. The other end of this dowel rod is then connected to the central sphere shown in Figures 21-22. This object serves as the base of the device. The sphere has eight holes specifically placed so that an octahedron can be formed when the dowel rods connected to the eight faces are inserted. For the octahedron to form properly, the dowel rods must all be cut to a length of 21.28 cm or $8\frac{3}{8}$ inches. This will form a fully contracted octahedron. To mimic a radial expansion of 10 mm, new dowel rods are cut

with an additional 10 mm in length. These dowel rods will have a length of 22.26 cm or $8\frac{49}{64}$ inches. The old rods are taken out and replaced with the newly cut rods. This technique is useful in that the radial expansion distance can continuously be changed and tested by simply replacing the dowel rods. An assembly was created in SolidWorks to validate the prototype's structure. Each individual part was able to connect together and form a fully contracted octahedron.

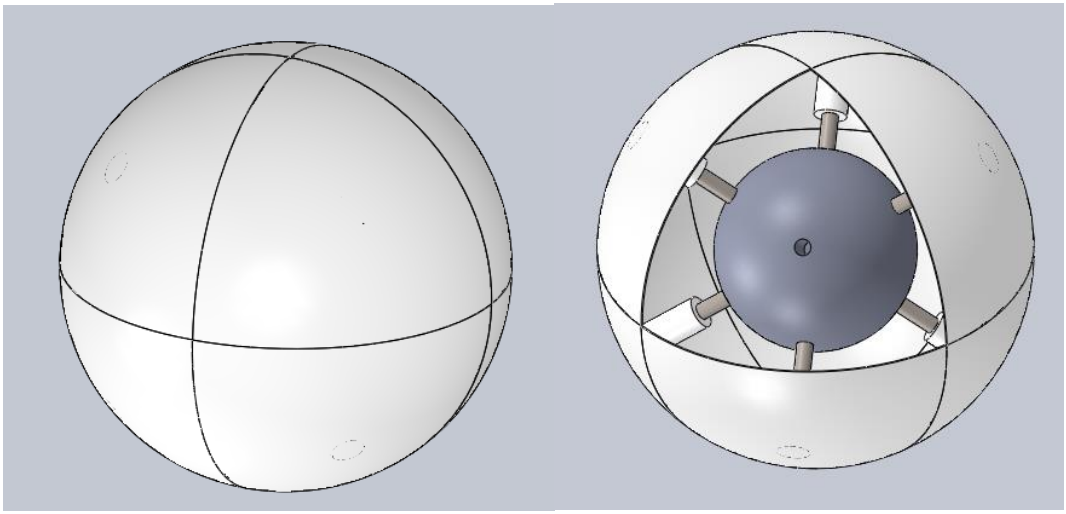

Figure 19. SolidWorks CAD model of the octahedron prototype.

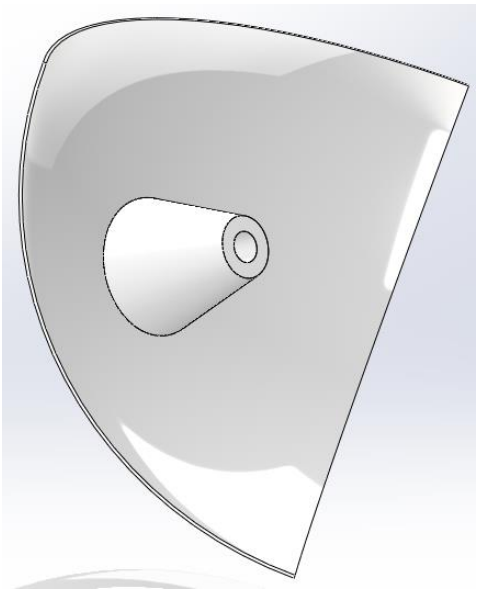

Figure 20. 1 of 8 face pieces for the octahedron prototype.

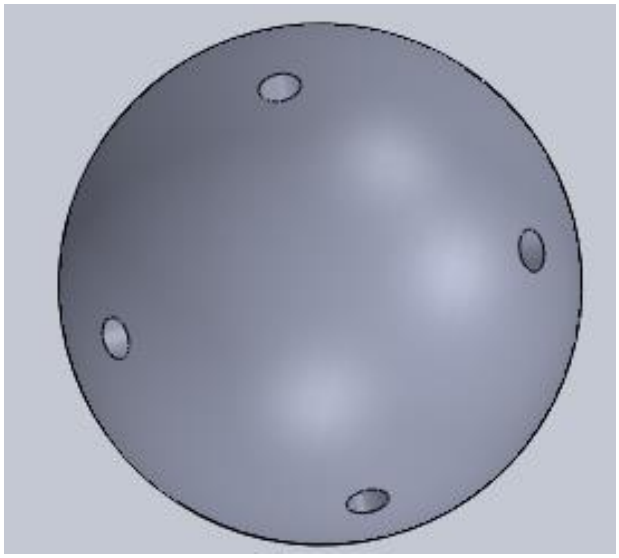

Figure 21. Central sphere that interconnects all of the eight face pieces.

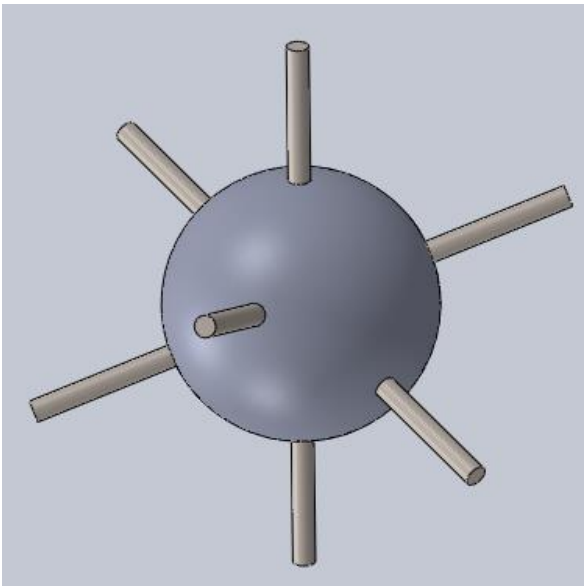

Figure 22. Central sphere showing interconnect-ability with dowel rods.

3. 3-D Printing and Coating

The device was brought to life via 3-D printing. Unfortunately, to be printable the parts had to be slightly modified. A 3-D printer prints from bottom-up, layer-by-layer. For this reason, each layer must be completely filled with material so it can serve as a base for the next layer to build on top of. When a hole exists, it is temporarily filled with support material. This support material can later be melted away and drained once the printing is done, thus forming the hole. For our parts, modifications were needed so that support material could be drained. The original designs did not allow a passage way for the support material to flow out of. These modifications were very simple, however. The face piece was adapted by splitting it straight down the middle and forming two smaller pieces. One of these split pieces is shown in Figure 23. The central sphere was altered using the exact same process. The part was split in half, as shown in Figure 26. Once printed, the original designs were restored by simply gluing the two

halves together. The manufactured parts are shown in Figures 24, 25, and 27. The parts were printed using Polylactic Acid (PLA) plastics. It is very important that our prototype closely resemble a PEC, as this is what was used in the simulations. To do this, we added a conductive nickel layer on top of the plastic. This process was done using MG Chemical's Super Shield product. The product comes in spray-paint-like can and the nickel coating is simply sprayed directly onto the eight face pieces.

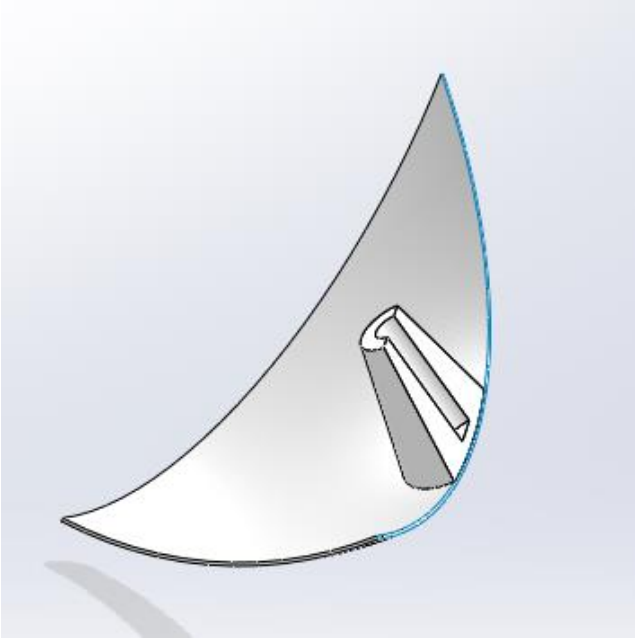

Figure 23. After result of splitting the face piece in half for 3-D printability.

Figure 24. Two halves of the 3-D printed face part.

Figure 25. Resulting face piece after assembling two halve pieces together.

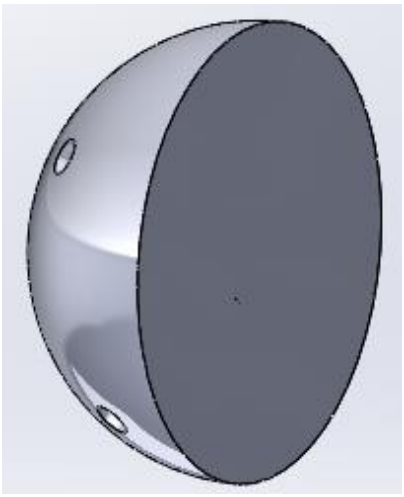

Figure 26. After result of splitting central connecting object in two halves.

Figure 27. Two halves of the 3-D printed central connector piece.

4. Test Setup

Testing was performed inside of an anechoic chamber located in the Electrical Engineering East building at Penn State University. The chamber is 10 ft. × 10 ft. × 20 ft. and fully shielded from unwanted electromagnetic signals. Measurements were taken using an E4408B Spectrum Analyzer capable of frequencies from 9 kHz to 26.5 GHz. Two collocated horn antennas were mounted on individual stands with height adjustability. The antennas were separated eight inches apart, mounted approximately five feet off the ground, and of VV polarization. Our target was positioned on a rotating table nine feet away and in line of sight (LOS) with the antennas. Low-dielectric Styrofoam was used to stabilize our target on the table. The down range view is shown in Figure 28.

Figure 28. Down range picture of the experimental setup used in the anechoic chamber.

5. Experimental Approach

A common methodology used for attaining RCS is the substitution method [9]. This technique simplifies the measurement process by utilizing well-understood calibration targets and their RCS properties. The process is well-derived in [1] as follows. The radar cross section of a target can be expressed in terms of the radar range equation as

$$\sigma = \frac{P_r}{P_t} \cdot \frac{(4\pi)^3 R^4}{G_t G_r \lambda^2} \tag{4.1}$$

where $\frac{4\pi^3 R^4}{G_t G_r \lambda^2}$ can be kept constant throughout the data collection process. The $\frac{P_r}{P_t}$ term is easily attainable by measuring the S_{21} parameter on a spectrum analyzer as

$$\frac{P_r}{P_t} = 10^{\frac{|S_{21}|^2}{10}} \tag{4.2}$$

The resulting RCS of a target then becomes

$$\sigma = 10^{\frac{|S_{21}|^2}{10}} \cdot \frac{(4\pi)^3 R^4}{G_t G_r \lambda^2} \tag{4.3}$$

When data are collected on a second target using the same experimental setup, the following equation is valid as the constants cancel each other out

(4.4)

$$\frac{\sigma_1}{\sigma_2} = \frac{10^{\frac{|S_{21}|^2{}_{(1)}}{10}}}{10^{\frac{|S_{21}|^2{}_{(2)}}{10}}} = 10^{\frac{|S_{21}|^2{}_{(1)} - |S_{21}|^2{}_{(2)}}{10}}$$

where the subscripts resemble targets 1 and 2. After some algebraic manipulation, the RCS term of the first target can be isolated as follows

$$\sigma_1 = S_{21(1)} - S_{21(2)} + \sigma_2 \tag{4.5}$$

where the RCS units are dBm^2 and the S_{21} units are dB. The second target is often a geometry whose RCS is well known and easy to compute. These geometries (e.g. sphere, flat plate, corner reflector) are frequently used for calibration purposes. Our experiments utilized a trihedral corner reflector geometry for this exact purpose. The formula for the reflector's RCS is given as

$$\sigma_{std} = \frac{4\pi L^4}{3\lambda^2} \tag{4.6}$$

where L represents the corner reflector's inside length [13]. As noted in [13], this equation must be used carefully as it assumes $\lambda << L$. At a frequency of 3.6 GHz, our wavelength is too large to use this approximation. To resolve this issue, the RCS of the corner reflector was computed using a Method of Moments (MoM) solver in FEKO. This is considered very accurate and can be used to solve for target RCS. The resulting simulation value for the corner reflector was an RCS of −6.42 dBm^2. In direct LOS, the calibration target had an S_{21} value of −47.07 dB.

The data collection procedure for the target consisted of four different measurements: (1) ϕ = 0°, θ = 0°- 360° while in the contracted state, (2) ϕ = 45°, θ = 0°- 360° while in the

contracted state, (3) ϕ = 0°, θ = 0°- 360° while in the expanded state, and (4) ϕ = 45°, θ = 0°- 360° while in the expanded state. The changes in θ occurred in five degree increments for a total

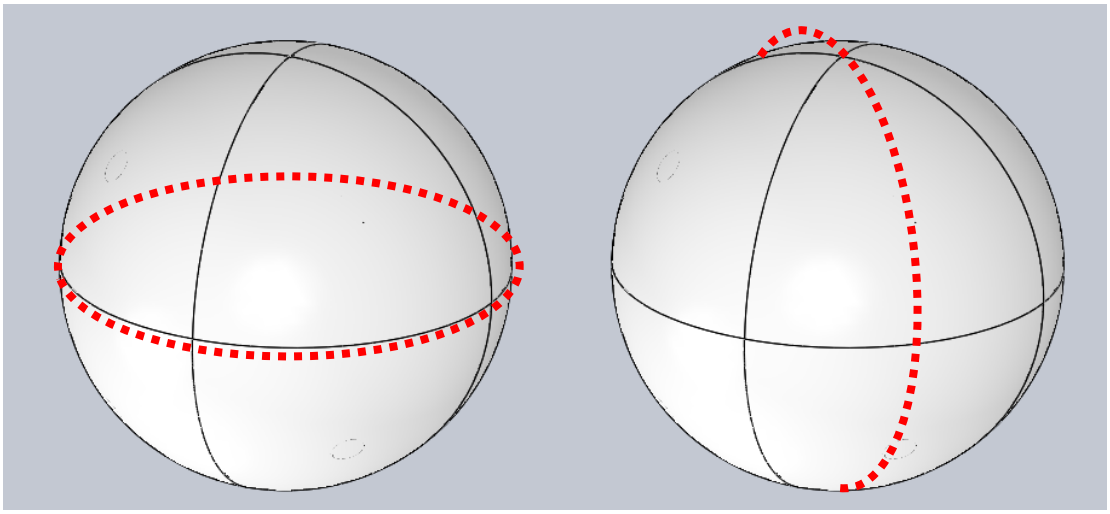

Figure 29. The two ϕ-cuts used during data collection. For both ϕ = 0° (left) and ϕ = 45° (right) a full 360° revolution was made around the θ-axis. Each was done in both the contracted and expanded state.

of 73 points per run. The rotations were controlled remotely using the rotating table holding the target. The changes in ϕ were performed by manually adjusting the target's LOS with the antennas.

The first collection of data was taken while the target was in a contracted state with ϕ = 0° and θ = 0°- 360°. Figure 30 shows a polar plot of the normalized data. It is worth noting that due to a minor error in the data gathering system, the first two values (θ = 0°, θ = 5°) are omitted for this run and not included on the polar graph. All other points on this plot as well as the remaining plots are without error. One of the main observations that can be made about this plot is that nulls exist in ninety degree increments at θ = 45°, 135°, 225°, and 315°. For a perfect sphere, we would see a smooth circle around one of the radial values in the plot and, thus, a constant RCS value at every direction. This lack of full consistency can be attributed to the

mechanical properties of the prototype. Though the target attempts to mimic a perfect sphere in its contracted state, it is unable to do so due to the physical limitations of the architecture. There

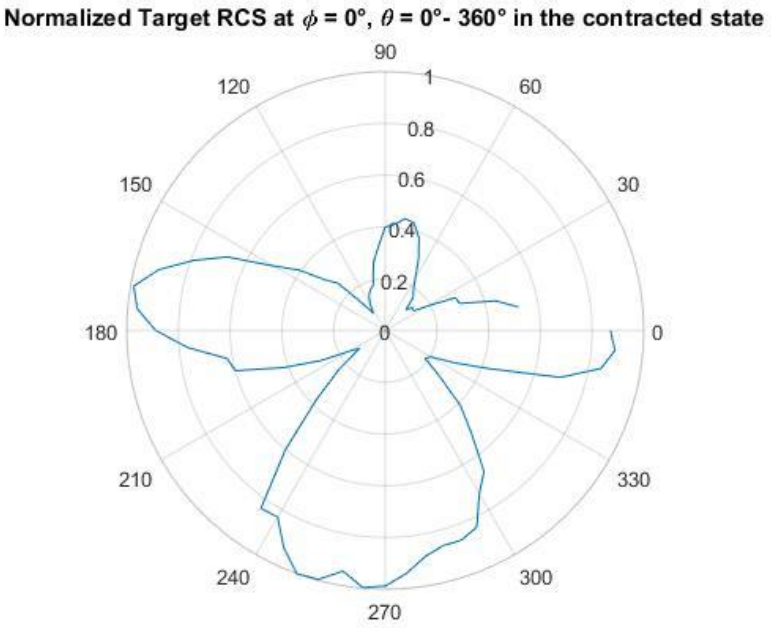

Figure 30. Normalized monostatic RCS of the target in its contracted state at ϕ = 0°.

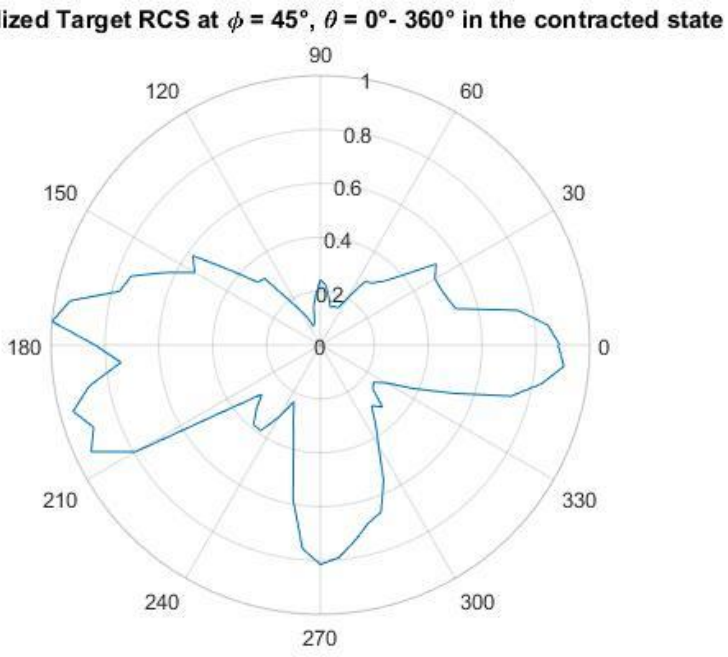

Figure 31. Normalized monostatic RCS of the target in its contracted state at ϕ = 45°.

still exists small gaps on the target that prevent consistent monostatic reflections. This issue will be discussed in detail later on. The second collection of data was performed by rotating the device 45 degrees along the ϕ-axis. There again appears to be nulls in ninety degree increments similar to the previous measurement. One of the major differences in this figure is the lack of a peak at θ = 90°. The consistent patterns are very telling of the effect that geometry has on scattering properties for an object. Fabricating this device to resemble a perfect sphere, geometrically, is of very high complexity. The slightest mishap in angle or dowel rod size will result in some type of geometric error and, thus, true RCS consistency will be lost. Figures 32 and 33 show the data collection for the expanded sphere at ϕ = 0° and ϕ = 45°, respectively. At ϕ = 0°, the target maintains a similar profile to that of Figures 30 and 31. Gaps are prevalent on the target at every point along this axis. This characteristic impacts the reflection profile of the target. The strongest reflections occurred when the front-facing orientation of our target possessed a vertical gap (e.g. θ = 0°, 90°, 180°, and 270°). Conversely, the weakest reflections

could be seen when only a horizontal gap was facing towards the antennas (e.g. θ = 45°, 135°, 225°, and 315°). We believe that the reasoning for this phenomenon relates to the polarization of the signal. Because the transmitted wave's electric field has a vertical orientation, it can easily pass through vertical gaps where it is then reflected off of internal faces and, further, reradiated out through the same gap towards the radar. When the horizontal gap is alone, it depolarizes the incoming electric fields thus preventing vertically polarized radiation from entering the gap and leaving it from the inside. The result of this is horizontally polarized radiation being backscattered towards the vertically polarized receiving antenna, thus causing the nulls in the data at these target locations. We again can see nulls in the RCS at 45-degree intervals.

For ϕ = 45° in the expanded state, we see peaks around 45° and 235°. When ϕ = 45°, the strongest returns are from angles where the antenna's LOS is directly aligned with the center of a face. The reasoning for this is rather straightforward; there are no gaps in the center of the faces and the reflected signal maintains vertical polarization. This occurrence can clearly be seen in Figure 33 as the RCS peaks around 45° and 225°. Unexpectedly, the RCS does not peak at the other expected increments (e.g. 135°, 315°). We believe that this is due to the unideal surface of the faces in these positions. Though the 3-D printing technique made the actual fabrication process simple, it is not ideal in terms of durability. The plastic was very fragile and became susceptible to cracking, as with these faces. Though some cracks formed and were not ideal, they gave us insight into the scattering profile of an unideal face. This is very important moving forward because it demonstrates the need for a robust target. Through-rubble testing will put fair amounts of pressure on the target and we now know that varying face profiles can lead to dissimilar results.

The experimental data are compared with the simulation data in Figures 34 and 35 for the expanded state. At ϕ = 0°, both sets of data show peaks near 0°, 90°, 180°, and 270°. The simulation, however, shows many more peaks in the areas between these intervals. One observation is that at the angles where the experimental data has nulls, the simulation data has very sharp, narrow peaks. This is a common occurrence in Physical Optics simulations and, often, is not something that will appear in the experimental data due to its very fine resolution properties. When the target is oriented at ϕ = 45°, the simulation data follows the same pattern as the experimental data. There are peaks in RCS at angles without visible gaps. The positions are located at 45°, 135°, 225°, and 315°. The experimental data are without two of these peaks for the reasons listed above.

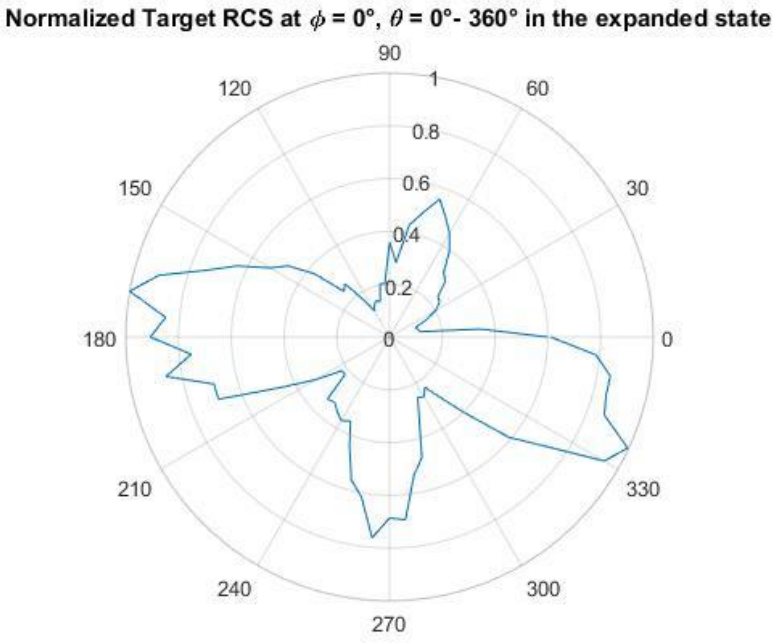

.

Figure 32. Normalized monostatic RCS of the target in its expanded state at ϕ = 0°.

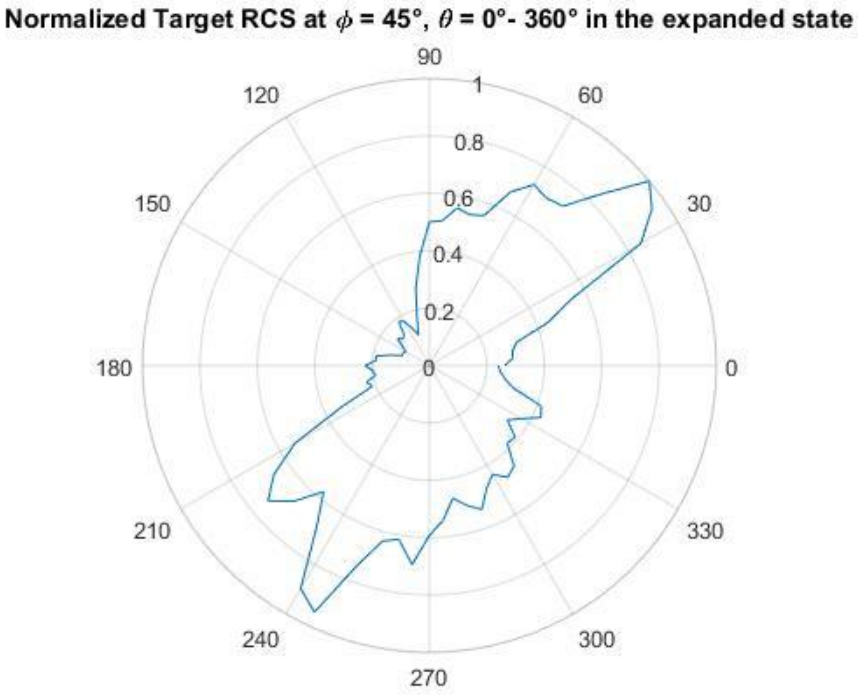

Figure 33. Normalized monostatic RCS of the target in its expanded state at ϕ = 45°.

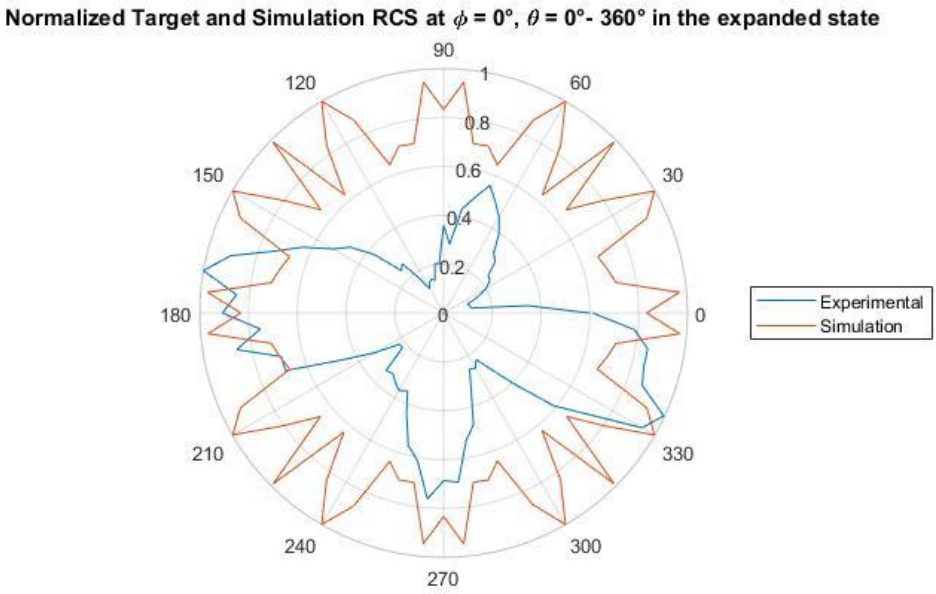

Figure 34. Comparison of experimental and simulated RCS in the expanded state at ϕ = 0°.

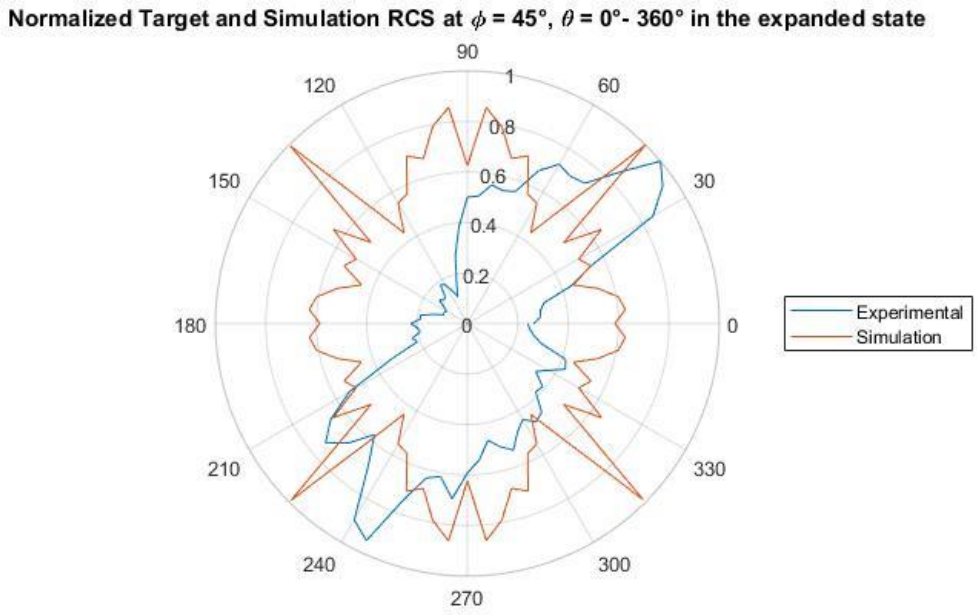

Figure 35. Comparison of experimental and simulated RCS in the expanded state at ϕ = 45°.

Figures 36 and 37 shows the raw RCS data at ϕ = 0° and 45°. When the data are not normalized, it can be seen how the experimental magnitudes are much less than the simulation magnitudes. The reason for this has to do with the conductivity of the materials used in each data set. The simulations assume a PEC material which is unattainable realistically though it can be closely approximated. For the experimental data, nickel coating was used which has a conductivity of 1.45 x 10^7 S/m. Future analysis may want to use a different material such as copper or silver which have conductivities of 5.76 x 10^7 S/m and 6.1 x 10^7 S/m, respectively [2]. This will give stronger reflections and better-approximate the PEC assumption in the simulations. It should also be noted that it is likely the nickel spray was not perfectly even along the surface of the target. Due to the spray-like application method, some areas may have had more nickel while others had less, causing different conductivities.

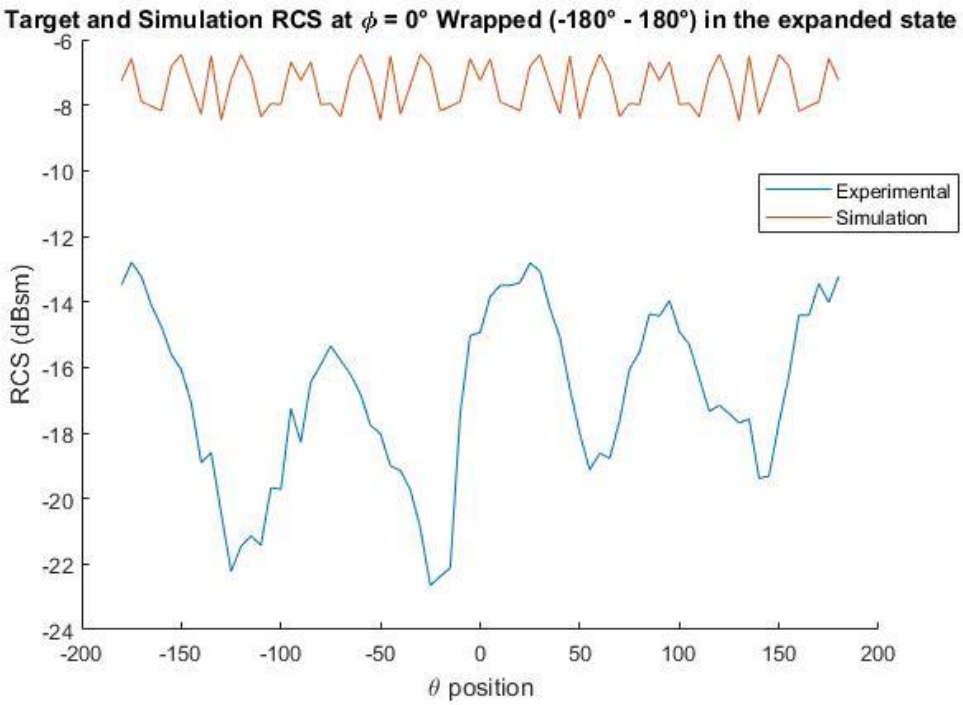

Figure 36. Raw RCS magnitudes when the target is in the expanded state at ϕ = 0°.

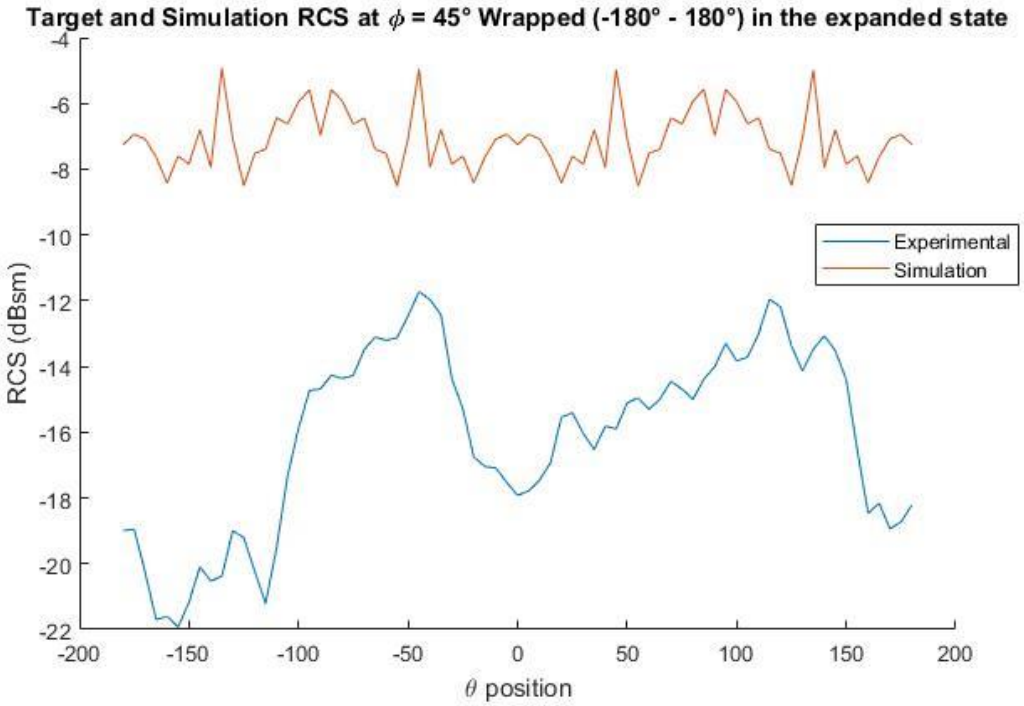

Figure 37. Raw RCS magnitudes when the target is in the expanded state at ϕ = 45°.

Chapter 5 – Concluding Remarks

The overall goal of this two-year long study was to develop an object that could be used as a calibration device for through-wall and through-rubble radar systems testing. These radar systems are specifically designed for the detection of humans and should exhibit human-like reflection properties. Another characteristic we strived towards attaining was aspect independency. An ideal calibration target is consistent in its returns and relatively easy to setup. If aspect independency is achieved, the calibration target possesses both of these characteristics.

Of the geometries we experimented with, we felt that the octahedron gave us the best results. We analyzed the geometry in both its contracted and expanded state. Simulation-wise, the target performed very well in aspect independency whilst in the contracted state. There was very little variation in the RCS along the surface of the target, thus showing a reflection behavior almost identical to a PEC sphere. Unfortunately, we were unable to maintain this consistency in our experiments. This outcome was useful, however, in that it exemplified the need for a very accurate design. To truly mimic a sphere in the contracted state, the design must align near-perfectly and have no noticeable gaps. This is complex due to the intricate geometry a sphere possesses. At 10 millimeters expansion, we analyzed the scattering effects in what we felt would be the largest expansion needed to mimic human breathing. At 3.6 GHz, we observed inconsistencies in the expanded target's RCS at different areas on the target due to the gaps that formed upon expansion.

Moving forward, there are some enhancements that can be made to improve upon this prototype that has been discussed. The first step would be to come up with a new design that interconnects the faces in a more efficient manner. The development steps we have taken so far were aimed at producing a model that was relatively inexpensive and could serve as a building

block for the finished product that is to come in the future. The use of dowel rods served this purpose but are not ideal for a finished product, and, only represent the target in a static state. The interconnection of the parts is extremely important because the target must resemble a perfect sphere as close as possible while in the contracted state. Another improvement I suggest would be in regards to the central connection points. The center sphere was unnecessarily heavy and put a fair amount of force on the faces when they were being mounted. The sole purpose of this feature is to bring all of the faces to a common connection point so they would align optimally upon assembly and retain the target's spherical geometry. The central object could either be hollowed out to lighten its weight or completely redesigned. The trouble in designing such a part is that it must connect eight different pieces and maintain symmetry. A decision also must be made on whether or not to address the gap issue. This study showed that the target loses RCS consistency as it expands radially. If the gaps are too severe, a possible solution to this would be covering the target with an elastic "sock-like" material. Essentially, this material would be flexible and tightly fit the entirety of the sphere much like a sock fits a foot. It would also need to be highly conductive and durable. If this is attainable, the gaps in the target would be masked and the expansion state would likely become much more consistent in RCS. Another thought also worth looking into is a new material for the faces. Ideally a face would be made of titanium or steel but this tends to be very expensive to fabricate. The 3-D printed plastic material used in this study works well now, but is very susceptive to deterioration in the future due to its brittle texture. Lastly, the target needs to be made more conductive. Though our method was useful for our purpose, the nickel paint did not do a fine enough job conducting energy. In the future, this could be done by hydroplating the faces with a copper or silver material.

The last phase of this design will involve the implementation of linear actuators as the object will shift from a static target to a dynamic one. This will truly encapsulate the mimicking of human respiration in a through-barrier setting. It will introduce micro-Doppler properties to the project and pave the way for a final fabrication stage. Though a fully integrated system will present challenges, the end product has great potential to be used for the improvement of human detecting systems and the standards by which those systems strive to meet.

Bibliography

1. Nicolaescu, L., & Oroian, T. (2001). Radar cross section. In *Telecommunications in Modern Satellite, Cable and Broadcasting Service, 2001. TELSIKS 2001. 5th International Conference on* (Vol. 1, pp. 65-68). IEEE.
2. Balanis, C. A. (1999). *Advanced Engineering Electromagnetics*. John Wiley & Sons.
3. Dogaru, T., Nguyen, L., and Le, C., "Computer models of the human body signature for sensing through the wall radar applications," US Army Research Laboratory Technical Report ARL-TR-4290 (2007).
4. Nezirovic, A., Tesfay, S., Valavan, A. S. E., & Yarovoy, A. (2008, October). Experimental study on human breathing cross section using UWB impulse radar. In *Radar Conference, 2008. EuRAD 2008. European* (pp. 1-4). IEEE
5. Nezirovic, A., Yarovoy, A. G., & Ligthart, L. P. (2006, May). Experimental study on human being detection using UWB radar. In *Radar Symposium, 2006. IRS 2006. International* (pp. 1-4). IEEE.
6. Kumar, A., Liang, Q., Li, Z., Zhang, B., & Wu, X. (2012, December). Experimental study of through-wall human being detection using ultra-wideband (UWB) radar. In *Globecom Workshops (GC Wkshps), 2012 IEEE* (pp. 1455-1459). IEEE.
7. Li, J., Zeng, Z., Sun, J., & Liu, F. (2012). Through-wall detection of human being's movement by UWB radar. *IEEE Geoscience and Remote Sensing Letters*, *9*(6), 1079-1083.
8. Aardal, Ø., Hamran, S.-E., Berger, T., Hammerstad, J., and Lande, T. S.. Radar cross section of the human heartbeat and respiration. in *Proc. 2010 IEEE Biomedical Circuits and Systems Conference (BioCAS)*, Paphos, Cyprus, Nov. 2010, pp. 53-57 (2010).
9. Aardal, Ø ., Hamran, S.-E., Berger, T., Hammerstad, J., and Lande, T. S.. Radar cross section of the human heartbeat and respiration in the 500 MHz to 3 GHz band. in *Proc. 2011 IEEE Radio and Wireless Symposium (RWS)*, Phoenix, AZ, Jan. 2011, pp. 422-425 (2011).
10. Kiriazi, J. E. (2010). Human cardiopulmonary recognition using close-range Doppler radar.
11. Fryar, C. D., Gu, Q., & Ogden, C. L. (2012). Anthropometric reference data for children and adults: United States, 2007-2010. *Vital and Health Statistics. Series 11, Data from the National Health Survey*, (252), 1-48.
12. Laidlaw, D. H., Trumbore, W. B., and Hughes, J. F. Constructive solid geometry for polyhedral. *ACM SIGGRAPH Computer Graphics* 20(4), 161-170 (1986).
13. Bufler, T. D. (2016). Radar Signature Analysis of Indoor Clutter and stationary Human Target Classification.
14. Wang, J., Ge, J., Zhang, Q., Li, X., Wei, M., Yang, Z., & Liu, Y. A. (2016). Radar cross-section measurements of ice particles using vector network analyzer. *AIP Advances*, *6*(9), 095310.